NASA/TM—2012-217696

Particle Trajectory and Icing Analysis of the E^3 Turbofan Engine Using LEWICE3D Version 3

Colin S. Bidwell
Glenn Research Center, Cleveland, Ohio

September 2012

NASA STI Program . . . in Profile

Since its founding, NASA has been dedicated to the advancement of aeronautics and space science. The NASA Scientific and Technical Information (STI) program plays a key part in helping NASA maintain this important role.

The NASA STI Program operates under the auspices of the Agency Chief Information Officer. It collects, organizes, provides for archiving, and disseminates NASA's STI. The NASA STI program provides access to the NASA Aeronautics and Space Database and its public interface, the NASA Technical Reports Server, thus providing one of the largest collections of aeronautical and space science STI in the world. Results are published in both non-NASA channels and by NASA in the NASA STI Report Series, which includes the following report types:

- TECHNICAL PUBLICATION. Reports of completed research or a major significant phase of research that present the results of NASA programs and include extensive data or theoretical analysis. Includes compilations of significant scientific and technical data and information deemed to be of continuing reference value. NASA counterpart of peer-reviewed formal professional papers but has less stringent limitations on manuscript length and extent of graphic presentations.

- TECHNICAL MEMORANDUM. Scientific and technical findings that are preliminary or of specialized interest, e.g., quick release reports, working papers, and bibliographies that contain minimal annotation. Does not contain extensive analysis.

- CONTRACTOR REPORT. Scientific and technical findings by NASA-sponsored contractors and grantees.

- CONFERENCE PUBLICATION. Collected papers from scientific and technical conferences, symposia, seminars, or other meetings sponsored or cosponsored by NASA.

- SPECIAL PUBLICATION. Scientific, technical, or historical information from NASA programs, projects, and missions, often concerned with subjects having substantial public interest.

- TECHNICAL TRANSLATION. English-language translations of foreign scientific and technical material pertinent to NASA's mission.

Specialized services also include creating custom thesauri, building customized databases, organizing and publishing research results.

For more information about the NASA STI program, see the following:

- Access the NASA STI program home page at *http://www.sti.nasa.gov*

- E-mail your question to *help@sti.nasa.gov*

- Fax your question to the NASA STI Information Desk at 443–757–5803

- Phone the NASA STI Information Desk at 443–757–5802

- Write to:
  STI Information Desk
  NASA Center for AeroSpace Information
  7115 Standard Drive
  Hanover, MD 21076–1320

NASA/TM—2012-217696

Particle Trajectory and Icing Analysis of the E^3 Turbofan Engine Using LEWICE3D Version 3

Colin S. Bidwell
Glenn Research Center, Cleveland, Ohio

Prepared for the
International Conference on Aircraft and Engine Icing and Ground Deicing
sponsored by the SAE International
Chicago, Illinois, June 13–17, 2011

National Aeronautics and
Space Administration

Glenn Research Center
Cleveland, Ohio 44135

September 2012

Acknowledgments

The author would like to thank Joseph Veres, Philip Jorgenson and Russell Claus of the NASA Glenn Research Center, Cleveland, Ohio for contributing the flow solution for the E^3 compressor and for aid in interpreting turbomachinery flow and particle transport physics.

This work was sponsored by the Fundamental Aeronautics Program at the NASA Glenn Research Center.

Level of Review: This material has been technically reviewed by technical management.

Available from

NASA Center for Aerospace Information
7115 Standard Drive
Hanover, MD 21076–1320

National Technical Information Service
5301 Shawnee Road
Alexandria, VA 22312

Available electronically at http://www.sti.nasa.gov

Particle Trajectory and Icing Analysis of the E^3 Turbofan Engine Using LEWICE3D Version 3

Colin S. Bidwell
National Aeronautics and Space Administration
Glenn Research Center
Cleveland, Ohio 44135

Abstract

Particle trajectory and ice shape calculations were made for the Energy Efficient Engine (E^3) using the LEWICE3D Version 3 software. The particle trajectory and icing computations were performed using the new "block-to-block" collection efficiency method which has been incorporated into the LEWICE3D Version 3 software. The $E^3$was developed by NASA and GE in the early 1980's as a technology demonstrator and is representative of a modern high bypass turbofan engine. The E^3 flow field was calculated using the NASA Glenn ADPAC turbomachinery flow solver. Computations were performed for the low pressure compressor of the E^3 for a Mach 0.8 cruise condition at 11,887 m assuming a standard warm day for three drop sizes and two drop distributions typically used in aircraft design and certification. Particle trajectory computations were made for water drop sizes of 5, 20, and 100 μm. Particle trajectory and ice shape predictions were made for a 20 μm Langmuir-D distribution and for a 92 μm Super-cooled Large Droplet (SLD) distribution with and without splashing effects for a Liquid Water Content (LWC) of 0.3 g/m^3 and an icing time of 30 min. The E^3 fan and spinner combination proved to be an effective ice removal mechanism as they removed greater than 36 percent of the mass entering the inlet for the icing cases. The maximum free stream catch fraction for the fan and spinner combination was 0.60 while that on the elements downstream of the fan was 0.03. The non-splashing trajectory and collection efficiency results showed that as drop size increased impingement rates increased on the spinner and fan leaving less mass to impinge on downstream components. The SLD splashing case yielded more mass downstream of the fan than the SLD non-splashing case due to mass being splashed from the upstream inlet lip, spinner and fan components. The ice shapes generated downstream of the fan were either small or nonexistent due to the small available mass and evaporation except for the 92 μm SLD splashing case. Relatively large ice shapes were predicted for internal guide vane #1 and rotor #1 for the 92 μm SLD splashing case due to re-impingement of splashed mass.

Introduction

Over the last several years work has been ongoing to develop tools to analyze aircraft configurations subjected to Super-cooled Large Droplet (SLD) conditions (Ref. 1) and High Ice Water Content (HIWC) conditions (Refs. 2 to 3). Both the SLD and HIWC environments contain conditions outside of the FAA Appendix C (Ref. 4) Certification Envelope. The SLD environment contains larger drops than the Appendix C envelope which impinge further back and which are subject to breakup and splash at impact. The HIWC environment contains large ice or mixed phase particles (>50 μm) in very high concentrations (~10 g/m^3) up to very high altitudes (~40000 ft). This HIWC environment has been responsible for many engine anomalies including engine roll backs and shutdowns. Work is underway to quantify the HIWC environment and to develop ground test facilities and computational tools to assess the sensitivity of various engines to the HIWC threat. New certification rules, which will require aircraft to fly safely through these conditions, are on the horizon. These new rules will generate new requirements for aircraft ice protection system design and certification and for the tools which aid in these processes.

The development of icing computational analysis tools which produce sufficiently accurate results in a reasonable amount of computational time for turbomachinery flows has been a major challenge (Refs. 5 and 6). The use of unsteady tools to simulate the flow and particle transport in the highly time dependent turbomachinery flows was seen as impractical and as possibly unnecessary. For this reason a methodology was developed at NASA Glenn which uses the steady flow assumption commonly used in turbomachinery design tools. These methods typically model blade rows as a single blade with circumferential symmetry and circumferentially averaged inflow and outflow boundary conditions which are generated from neighboring blade rows. These methods typically march through the turbomachinery calculating steady flow for each blade using the upstream blade outflow boundary data and the downstream inflow boundary data for the inflow and outflow boundary conditions respectively. Several passes through the engine to achieve convergence are typically employed by these methods.

The newly developed NASA Glenn "block-to-block" icing analysis method follows the same logic used in these steady flow turbomachinery flow analysis tools. Droplet transport and ice shape calculations are generated for each blade row using steady, single blade flow solutions and the outflow droplet size, concentration, and particle velocity data from the upstream blade row as inflow data. The upstream blade outflow droplet concentration and droplet velocities are circumferentially averaged before being passed to the downstream blade row as an inflow boundary condition. This "block-to-block" method was incorporated into the NASA Glenn 3D ice accretion tool LEWICE3D Version 3 (Ref. 7).

The E^3 engine (Refs. 8 to 10) was selected as a test case for the newly developed "block-to-block" method incorporated into LEWICE3D Version 3. The E^3 was developed by NASA and GE in the early 1980's as a technology demonstrator. The engine was chosen because it is representative of a modern high bypass turbofan engine, the geometry and experimental data were publicly available and flow solutions were readily available.

The analysis was done in two parts. The first part was a particle analysis for 5, 20, and 100 μm particles to explore the nature of particle flow through the E^3. The particles used in this analysis were water droplets but they also could represent spherical ice particles which have a similar density. Throughout the study the term particle and drop are used interchangeably and are meant to imply particles with the same drag characteristics as water drops with a density equal to that of water. The 5 and 20 μm particles are typical of particle sizes used in Appendix C analysis. The 100 μm particle is a typical particle size for both SLD and HIWC. The second part was an icing analysis using two water droplet distributions typically used in aircraft design and certification. The first distribution was a 20 μm Appendix C distribution. The second distribution used was a 92 μm SLD distribution. The SLD droplet distribution was obtained from measurements in the NASA Glenn Icing Research Tunnel during droplet impingement tests (Ref. 11). The SLD calculations were done with the SLD splashing model turned off and with it turned on to quantify the effect of droplet splashing on the icing characteristics of the E^3. The SLD splashing results may provide some insight into the HIWC ice crystal environment throughout the engine. It is thought that the large ice crystals contained in the HIWC environment probably breakup into smaller particles during impact much like the large SLD drops breakup into smaller drops upon impact. It is also important to note that the E^3 flight condition chosen for the analysis (cruise at Mach 0.8, 11,887 m) is typical of HIWC conditions but not of SLD or Appendix C icing conditions, which typically occur at lower altitudes and speeds. The authors believe the icing analysis has merit even though the conditions chosen were not consistent with actual Appendix C or SLD conditions. The study represents an initial step in exploring the particle and icing characteristics of a turbofan compressor and it illustrates the newly developed capability of the LEWICE3D Version 3 software.

Nomenclature

d	droplet diameter, μm
E^3	Energy Efficient Engine
HTC	Heat Transfer Coefficient, $W/m^3/K$

IGV Inlet Guide Vane
LWC Liquid Water Content, g/m^3
MVD Median Volume Diameter, μm
β Collection efficiency

Analytical Method

Grid and Flow Calculations

The ADPAC flow solver (Refs. 12 to 14) was used to generate the flow solution for the analysis. The ADPAC code is a three-dimensional, finite volume based, Reynolds Averaged Navier-Stokes flow solver. The code computes flows on complex propulsion system configurations using multi-block body fitted grids. The method employs a "mixing-plane" procedure to pass boundary condition data between grid blocks for the steady state flows. The code supports parallel computing and uses a Baldwin-Lomax based turbulence model.

LEWICE3D

The LEWICE3D ice accretion code was used for the drop trajectory and icing analysis. The grid based code incorporates droplet trajectory, heat transfer and ice shape calculation into a single computer program. The code can handle generic multi-block structured grid based flow solutions, unstructured grid based flow solutions, simple Cartesian grids with surface patches, and adaptive grids with surface patches. The latter two methods allow the use of generic panel code input which, when combined with LEWICE3D, is a computationally efficient method for generating ice shapes. The code can handle overlapping and internal grids and can handle multiple planes of symmetry. Calculations of arbitrary streamlines and trajectories are possible. The code has the capability to calculate tangent trajectories and impingement efficiencies for single drops or drop distributions using area based collection efficiency methods. Ice accretions can be calculated at arbitrary regions of interest in either a surface normal or tangent droplet trajectory direction. The program can run on a variety of single processor and parallel computers, including Unix, Linux, and Windows (Microsoft Corporation) based systems.

Version 3 of the LEWICE3D software, which incorporates several new features, was used for the analysis. These features include a new particle splash and bounce algorithm, a new geometry handling scheme which allows complex mirroring, transformation and relative motion of input grid blocks and a new algorithm which calculates block-to-block collection efficiencies. The capability to calculate particle trajectories in rotating reference frames was also added (Ref. 5). These new additions will enable users to analyze SLD conditions and to calculate collection efficiency with particle splash and bounce effects through turbomachinery.

The "block-to-block" collection efficiency methodology in LEWICE3D was used to calculate collection efficiencies and ice shapes for the low pressure compressor of the E^3 for a cruise condition (Mach 0.8, at an altitude of 11,887 m assuming a standard warm day). The flow solution was obtained using the NASA Glenn ADPAC flow solver. The work presented in this paper represents calculations on the E^3 low pressure compressor for several drop sizes and droplet distributions.

Analysis

The E^3 analysis included the calculation of flow, particle trajectories and ice accretions. The results for the flow are presented along with particle analysis for 5, 20, and 100 μm drop sizes. Ice accretion calculations were made for 2 droplet distributions typically used in aircraft design and certification. These distributions included an Appendix C based 7 bin Langmuir-D distribution with a Median Volume Diameter (MVD) of 20 μm (Table 1) and a 10 bin SLD based distribution with an MVD of 92 μm

(Table 2). Ice accretion calculations were made for the SLD distribution with and without splashing. The ice accretion calculations were made at six locations in the E^3 low pressure compressor. These included the inlet lip, splitter lip #1, splitter lip #2, and the 25 percent span location on the fan blade, inlet guide vane #1, and rotor #1 shown in Figure 1.

The grid structure used for the flow and particle analysis is shown in Figure 1. The grid contained 12 structured, abutted grid blocks with a total of 327,583 nodes. The steady, viscous flow solution was generated for a Mach 0.8 cruise condition at 11,887 m assuming a standard warm day. Flow vectors along the centerline of the axi-symmetric solution are shown in Figure 2.

Figure 3 shows the collection efficiency (β) and particle trajectory results for the 5 μm case. Collection efficiency is a non-dimensional measure of the water flux for a surface and is dependent upon the amount of convergence or dispersion of particles in a flow and the orientation of the surface relative to the droplet paths. A collection efficiency of one implies the surface water loading is equal to the free stream water loading. A value less than one means the surface water loading is less than the free stream water loading and a value greater than one imply that the surface water loading is greater than the free stream level. From the collection efficiency, drop trajectory and drop trajectory impact points shown in Figures 3(a) to (d) we can see that impingement occurs throughout the low pressure compressor. The droplet trajectories are shown in the rotating reference frame of the fan. The droplet trajectory impact point plot (3d) displays the impact locations for the droplets calculated in each of the blocks for the "block-to-block" method. This plot illustrates the density and location of the impacting drops used in the "block-to-block" method. The peak value of collection efficiency for the fan was 1.2 (Table 3) and occurred on leading edge of the pressure side of the fan blade near the blade root. The free stream catch fractions were relatively small for the 5 μm for the various components shown in Table 3 (<6 percent). The free stream catch fraction was defined as the ratio of the mass impinging on a component divided by the mass available in the free stream for an area equal to the area bounded by the highlight of the inlet lip. The elements of interest listed in Table 3 (spinner, fan blade, splitter lip #1, IGV #1, rotor #1 and splitter lip #2) removed 11 percent of the mass entering the inlet with the spinner and fan removing the largest portion (7 percent).

The collection and particle trajectory results for the 20 μm case are show in Figure 4. As for the 5 μm drop the 20 μm drop revealed impingement throughout the low pressure compressor although the impingement area was larger for the 20 μm drop (Figs. 3(d) and 4(d)). For most of the components the impingement rates were higher for the 20 μm drop than for the 5 μm drop due to drop inertia. Larger particles, which have larger inertia, are more resistive to changes in direction due to flow gradients than smaller particles which results in the larger particles being less apt to avoid obstacles. The maximum value of collection efficiency for the fan was 1.54 (Table 4) and it occurred on leading edge of the pressure side of the fan blade near the root of the blade. The elements of interest listed in Table 4 (spinner, fan blade, splitter lip #1, IGV #1, rotor #1 and splitter lip #2) removed 49 percent of the mass entering the inlet. The fan and spinner elements removed most of this mass (47 percent).

The collection and particle trajectory results for the 100 μm case are show in Figure 5. Impingement is visible from Figure 5(d) for the bypass region but not aft of IGV #1 for the inner flow path. The 100 μm drops were not able to negotiate the flow path between the IGV #1 blades due to droplet inertia and a higher relative angle-of-attack. From the IGV #1 inflow particle and air velocity vectors shown in Figure 6 we can see that that the 100 μm drop had a larger relative angle-of-attack than 5 μm particle or the air. This higher relative angle-of-attack and inertia of the larger 100 μm drops results in a 100 percent collision rate with IGV #1. The maximum collection efficiency on the fan blade was 0.92 and occurred on the aft end of the fan blade near the root. The elements of interest listed in Table 5 (spinner, fan blade, splitter lip #1, IGV #1, rotor #1 and splitter lip #2) removed 73 percent of the mass entering the inlet with the spinner and fan removing the largest portion (72 percent).

The collection efficiency results for the 20 μm Langmuir-D distribution are shown in Figure 7. The results are similar to those for the single 20 μm particle. The impingement limits are farther aft on the inlet lip and spinner for the distribution than for the single drop size case due to the presence of larger

drops in the distribution. The maximum collection efficiency on the fan blade (Table 6) was also greater for the distribution case than that for the single drop size case due to the presence of larger drops in the distribution case (1.9, 1.5 respectively). The maximum occurred on the leading edge of the pressure side of the fan blade near the blade root. The amount of mass impinging on the elements of interest in Table 6 was also similar to the 20 μm single drop case (47 and 49 percent, respectively). The distribution case yielded a small amount of mass entering the inner core (0.2 percent of that entering the inlet). This was due to the presence of small drops in the distribution case which were able to negotiate the blade passages close to the inner wall and enter the inner core.

Figure 8 presents the collection efficiency results for the 92 μm SLD distribution without splashing. The magnitude of collection efficiency and the extent of impingement on the inlet lip and spinner are larger than for the 20 μm Langmuir-D case due to the larger drops present in the SLD distribution. The impingement rates and maximum collection efficiencies for the 92 μm distribution case were similar to those for the single 100 μm drop case except that the distribution case generated impingement on the elements aft of IGV #1. This was due to the presence of smaller drops in the distribution case which were able to negotiate the passages between the upstream blades. The maximum collection efficiency on the fan blade was 1.14 and occurred on the aft end of the fan blade near the root. The elements of interest listed in Table 7 (spinner, fan blade, splitter lip #1, IGV #1, rotor #1 and splitter lip #2) removed 67 percent of the mass entering the inlet with the spinner and fan removing the largest portion (66 percent). As for the 20 μm Langmuir-D distribution case a small amount of mass was calculated entering the inner core (0.03 percent of that entering the inlet).

The SLD 92 μm collection efficiency results for splashing are shown in Figure 9 and in Table 8. The SLD splashing model results in an increase in mass loss as the impingement limits are approached for the inlet lip and spinner over the non-splashing result shown in Figure 8. The fan blade impingement characteristics for the SLD splashing and non splashing cases were markedly different. The splashing case shows a large amount of mass loss near the leading edge of the fan blade toward the root. The splashing case also shows higher levels of collection efficiency on the trailing edge of the fan blade near the root than the non-splashing case due to re-impingement. The mass collected on the fan blade is smaller for the SLD splashing case than for the non-splashing case due to splashing (91.466 and 134.717 g/s, respectively). The percentage of mass entering the inlet which was collected on the elements of interest listed in Table 8 (spinner, fan blade, splitter lip #1, IGV #1, rotor #1 and splitter lip #2) was much smaller for the splashing case than for the non-splashing case due to splashing (39 and 67 percent, respectively). The splashing case also predicted more mass entering the core than the non-splashing case (6.946 and 0.061 g/s, respectively). This additional mass was comprised of a large number of small particles generated by the breakup of the larger SLD drops during impact.

The ice accretion results for several elements of interest in the E^3 compressor are presented in Figures 10 to 23. These results include collection efficiency, heat transfer coefficient and ice shape predictions for the inlet lip, fan blade, splitter lip #1, IGV #1, rotor #1, and splitter lip #2. The predictions were generated for an LWC of 0.3 g/m^3, an icing time of 30 min for a 20 μm Langmuir-D distribution, a 92 μm SLD distribution without splashing and a 92 μm SLD distribution with splashing.

From the collection efficiency results for the inlet lip in Figure 10 we can see that the SLD droplet distributions yield larger maximum collection efficiencies and extents of impingement than the Langmuir-D distribution due to the presence of larger drops. The SLD splashing model also generates lower impingement efficiencies than the SLD non-splashing model.

The fan blade collection efficiency distributions are shown in Figure 11. The SLD non-splashing case yielded the largest overall collection. The overall collection was defined here as the area under the collection efficiency curve. The SLD splashing case resulted in lower collection efficiency at the leading edge of the fan blade than for the SLD non-splashing case due to drop splashing and a higher level of collection efficiency at the trailing edge due to re-impingement of mass. The SLD cases showed an increase in collection efficiency towards the trailing edge of the fan blade while the 20 μm Langmuir-D distribution was relatively flat.

The collection efficiency distributions for splitter lip #1 are shown in Figure 12. The 20 μm Langmuir-D distribution generated the highest collection efficiency on splitter lip #1 although the level was small ($\beta < 0.11$). From Tables 6 to 8 we see that the impingement rates were also higher for the smaller Langmuir-D drop size case than for the SLD non-splashing and splashing cases (0.645, 0.401, and 0.105 g/s, respectively). The SLD splashing case revealed a large loss in mass over the non-splashing case due to droplet splashing. The smaller impingement rates of the larger 92 μm non-splashing SLD case as compared to the smaller 20 μm Langmuir-D case was counter-intuitive. Generally larger drops produce larger collection efficiency on static objects. Two contributing factors to this result are postulated. The first is that there is less mass available for impingement at the inflow to splitter lip #1 for the larger drops than for the smaller drops because the fan and spinner have removed more of the mass for the larger drops. The fan and spinner removed 67 percent of the mass entering the inlet for the SLD non-splashing case as opposed to 47 percent for the 20 μm Langmuir-D case. It was also thought that the reduction in collection efficiency could be due in part to a sweep effect caused by the swirl of the particle paths by the fan. From Figure 6 we can see that the larger 100 μm drops have a larger initial cross flow component of velocity relative to splitter lip #1 as compared to the smaller 5 μm drops. This larger cross flow angle or relative sweep could result in a reduction of collection efficiency as it does for external swept wing droplet impingement (Ref. 15).

The collection efficiency results for IGV #1 are shown in Figure 13 and in Tables 6 to 8. The SLD splashing case shows the largest impingement rate due to re-impingement of mass splashed from upstream components. Impingement on both the pressure and suction sides of IGV #1 were calculated for all of the distribution cases. For the non-splashing cases most of the impingement was on the upper suction surface due to the low relative angle-of-attack of the inflow particles (Fig. 6). The 92 μm SLD non-splashing case yielded a smaller impingement rate than the 20 μm Langmuir-D case (0.9 and 1.1 percent of the mass entering the inlet, respectively) because of the smaller available mass due to larger impingement on upstream components for the 92 μm SLD case. The large amount of re-impingement on the trailing edge of the pressure surface for the SLD splashing case was comprised of the droplets which were splashed from the pressure side of the fan blade and hence entered the IGV #1 at a higher relative angle-of-attack than for the non-splashed drops.

Rotor #1 collection efficiency results are shown in Figure 14. For all three cases there was impingement on the entire length of the pressure side of rotor #1 and on the leading portion of the suction side. The relative amount of impingement was small for the non-splashing cases ($\beta < 0.06$). As for IGV #1 the 92 μm SLD non-splashing case yielded a smaller impingement rate than the 20 μm Langmuir-D case (0.06 and 0.55 percent of the mass entering the inlet, respectively) because of the smaller available mass for the 92 μm SLD case. We can see that for the rotor #1 case the SLD splashing case yields 1165 percent (Tables 7 and 8) more impingement than the SLD non-splashing case due to re-impingement. The re-impinging mass for the rotor was a combination of the mass splashed from the upstream components including the spinner, the fan, and IGV #1.

The collection efficiency results for splitter lip #2 are shown in Figure 15 and Tables 6 to 8. The maximum collection efficiencies ($\beta < 0.08$) and free stream catch fractions for the splitter #2 lip were small for all of the cases (<0.0013). The 92 μm SLD non-splashing case yielded a smaller impingement rate than the 20 μm Langmuir-D case (0.03 and 0.17 percent of the mass entering the inlet, respectively) because of the smaller available mass for the 92 μm SLD case. The SLD splashing case yields 443 percent (Tables 7 and 8) more impingement than the SLD non-splashing case due to re-impingement.

The heat transfer coefficient distributions for the inlet lip, splitter lip #1 and splitter lip #2 are shown in Figure 16. The largest values were observed for splitter lip #1 due to the smaller leading edge radius of curvature for this element. The smaller leading edge radius for this element translates into large velocity gradients which yield higher heat transfer coefficients than for the other two elements. All three of the elements exhibit transition both above and below the stagnation point evidenced by sharp increase in the heat transfer coefficient on either side of the stagnation point. The splitter lip #1 heat transfer coefficient distribution shows the earliest transition due to its sharper leading edge.

Figure 17 shows the results for the fan blade, IGV #1 and rotor #1. The highest heat transfer coefficients are realized by IVG #1 due to its smaller leading edge radius of curvature. Transition occurs immediately for all three of the elements due to the relatively small leading edge radius of curvature of the elements.

Ice shape predictions for the inlet lip are shown in Figure 18. The SLD conditions generated the largest ice shapes due to the higher collection efficiencies produced by the larger drops present in the SLD distributions. The non-splashing SLD case results in a larger shape than the splashing SLD case due to mass loss by droplet splashing. The higher water loading for the SLD cases results in a glaze condition with small horns evident in the figure. The smaller 20 μm Langmuir-D generates a lower water loading and a shape more indicative of a mixed condition.

The ice shape comparisons for the fan blade are shown in Figure 19. The ice shapes for the non-splashing cases were very similar with the smaller 20 μm Langmuir-D case generating a smaller trailing edge ice thickness due to lower collection efficiencies than for the SLD non-splashing case. The effect of mass loss at the leading edge due to splashing is evident from the splashing and non-splashing ice shapes. Also from the figure one can see the increased mass at the trailing edge for the SLD splashing case over the SLD non-splashing case due to re-impingement.

The ice shape predictions for splitter #1 are shown in Figure 20. The largest ice shapes were produced by the 20 μm Langmuir-D case which also showed the highest collection efficiencies. The SLD splashing case is markedly smaller than the SLD non-splashing case due to drop splashing and the resulting mass loss.

The ice shapes for IGV #1 are shown in Figure 21. The largest ice shape was produced by the splashing SLD shape due to the larger impingement rates for this case. The SLD splashing case generated a large amount of trailing edge ice on the pressure side of the blade due to re-impingement. The SLD non-splashing produced a small ice accretion due to the low overall collection efficiency for the case and evaporation. All of the ice shapes for IGV #1 were affected significantly by evaporation. The SLD non-splashing case lost 69 percent while the SLD splashing case lost 19 percent of the impinging mass due to evaporation. The 20 μm Langmuir-D case lost 48 percent of the mass due to evaporation.

Ice shape predictions for rotor #1 are shown in Figure 22. The ice shape produced for the SLD splashing case was relatively large while those for the SLD non-splashing and 20 μm Langmuir-D cases were small. The percent evaporation for the non-splashing SLD case was 100 percent while that for the splashing case was 15 percent. The 20 μm Langmuir-D case lost 70 percent of the mass due to evaporation.

The splitter lip #2 ice accretions are shown in Figure 23. Relatively small accretions were generated for the SLD splashing and 20 μm Langmuir-D cases. The largest ice shape was produced for the SLD splashing case due to re-impingement of mass splashed from upstream components. The SLD non-splashing case, which showed some impingement, lost 100 percent of the impinging mass due to evaporation. The evaporation for the SLD splashing case was 58 percent while that for the 20 μm Langmuir-D case was 79 percent.

Conclusion

Predictions for droplet impingement and ice accretion were generated for the E^3 low pressure compressor using the new “block-to-block” collection efficiency method incorporated into LEWICE3D Version 3 and a flow solution from the ADPAC flow solver. The non-splashing trajectory and collection efficiency results showed that as drop size increased impingement rates increased on the spinner and fan leaving less mass to impinge on downstream components. The SLD splashing case yielded more mass downstream of the fan than the SLD non-splashing case due to mass being splashed from the upstream inlet lip, spinner and fan components. The maximum free stream catch fraction for the fan and spinner combination was 0.60 while that on the elements downstream of the fan was 0.03.

The ice shapes calculated for the E^3 were highly dependent upon particle size, evaporation and splashing. The ice accretions for the inlet lip and fan blade were relatively large and were similar in size for the Langmuir-D and SLD distributions. The E^3 fan and spinner combination proved to be a good collector removing greater than 36 percent of the mass entering the inlet for the distribution cases. The ice shapes predicted for the components downstream of the fan were relatively small due to the availability of mass and evaporation except for the IGV #1 and rotor #1 SLD splashing cases. The ice shapes or the IGV #1 and rotor #1 SLD splashing cases were relatively large due to the re-impingement of mass splashed from upstream components.

References

1. Bond, T., Potapczuk, M., Miller, D., "Overview of SLD Engineering Tool Development," AIAA-2003-386, Jan. 2003.
2. Mason, J; Strapp, W and Chow, P; "The Ice Particle Threat to Engines in Flight," 44th AIAA Aerospace Sciences Meeting, v4, 2006, pp. 2445-2465.
3. Mazzawy R.S., Strapp J.W.; "Appendix D – An Interim Icing Envelope; SAE 2007-01-3311; *SAE 2007 Aircraft and Engine Icing International Conference*; Seville, Spain, November 2007.
4. Federal Aviation Regulation, Part 25, "Airworthiness Standard: Transport Category Airplanes, Appendix C," DOT, FAA, 1974, rev. 1982.
5. Hamed, A., Das, K., Basu, D., "Effect Numerical Simulations of Ice Droplet Trajectories and Collection Efficiency on Aeroengine Rotating Machinery," AIAA 2005-1248, 2005.
6. Wright, W., Jorgenson, P., Veres, J., "Mixed Phase Modeling in GlennICE with Application to Engine Icing," AIAA-2010-7674, 2010.
7. Bidwell, C.S., Potapczuk, M.G., "Users Manual for the NASA Lewis Three-Dimensional Ice Accretion Code (LEWICE3D)," NASA TM-105974, December 1993.
8. Cline, S.J., Halter, P.H., Kutney, J.T., and Sullivan, T.J., "Energy Efficient Engine: Fan and Quarter-Stage Component Performance Report," NASA CR 168070, Jan. 1983.
9. Bridgeman, M.J., Cherry, D.G., and Pedersen, J., "NASA/GE Energy Efficient Engine Low Pressure Turbine Scaled Test Vehicle Performance Report," NASA CR 168290, Jul. 1983.
10. Rowe, R.K. and Kuchar, A.P., "Energy Efficient Engine (E 3) Scaled Mixer Performance Report - Final Report," NASA CR 167947, Nov. 1982.
11. Papadakis, M., Elangonan, G., Fruend, G., Breer, M., Whitmer, L., "An Experimental Method for Measuring Water Droplet Impingement Efficiency on Two-and Three-Dimensional Bodies," NASA CR 4257, DOT/ FAA/CT-87/22, Nov. 1989.
12. Adamczyk, J.J., Celestina, M.L., and Beach, T.A., "Simulation of Three-Dimensional Viscous Flow Within a Multistage Turbine," ASME Paper 89-GT-152, 1989.
13. Hall, E., Heidegger, N., Delaney, R., "ADPAC v1.0 – Users's Manual," NASA CR 1999-206600.
14. Hall, E., Delaney, R., Lynn, S., Veres, J., "Energy Efficient Low Pressure Subsystem Aerodynamic Analysis," NASA TM 1988-208402.
15. Bidwell C.S and Mohler S.R. "Collection Efficiency and Ice Accretion Calculations for a Sphere, a Swept MS(1)-317 Wind, a Swept NACA 0012 Wing Tip, an Axisymmetric Inlet and a Boeing 737-200 Inlet," NASA TM-106821, 1995.

TABLE 1.—LANGMUIR-D DROPLET DISTRIBUTION FOR AN MVD OF 20 μm

D, μm	% LWC
6.2	0.05
10.4	0.1
14.2	0.2
20	0.3
27.4	0.2
34.8	0.1
44.4	0.05

TABLE 2.—SLD DROPLET DISTRIBUTION FOR AN MVD OF 92 μm

D, μm	% LWC
10.96046	0.05
27.59405	0.1
51.17964	0.2
92.18893	0.3
136.2497	0.2
179.8884	0.1
230.625	0.03
283.3301	0.01
339.5112	0.005
391.7745	0.005

TABLE 3.—E^3 IMPINGEMENT STATISTICS FOR A DROP SIZE OF 5 μm

Element	β_{max}	Impingement rate, g/s	Free stream catch fraction
Free stream capture tube (assuming capture area of 3.26 m^2)	1	237.397	1
Inlet lip	0.300	2.186	0.0092
Inlet capture	1.248	189.932	0.8000
Spinner	0.034	0.338	0.0014
Fan blade	1.200	13.655	0.0575
Splitter lip #1	0.305	1.134	0.0048
IGV #1	0.518	4.757	0.0200
Rotor #1	2.030	0.904	0.0038
Splitter lip #2	0.004	0.010	0.0000
Inner core	0.513	3.487	0.0147

TABLE 4.—E^3 IMPINGEMENT STATISTICS FOR A DROP SIZE OF 20 μm

Element	β_{max}	Impingement rate, g/s	Free stream catch fraction
Free stream capture tube (assuming capture area of 3.26 m^2)	1	237.397	1
Inlet lip	0.671	25.395	0.1070
Inlet capture	1.057	190.128	0.8000
Spinner	0.174	5.110	0.0210
Fan blade	1.540	83.894	0.3530
Splitter lip #1	0.183	1.136	0.0048
IGV #1	0.420	2.286	0.0096
Rotor #1	0.160	0.612	0.0026
Splitter lip #2	0.006	0.046	0.0002
Inner core	0	0	0

TABLE 5.—E^3 IMPINGEMENT STATISTICS FOR A DROP SIZE OF 100 μm

Element	β_{max}	Impingement rate, g/s	Free stream catch fraction
Free stream capture tube (assuming capture area of 3.26 m^2)	1	237.397	1
Inlet lip	0.950	85.570	0.3600
Inlet capture	1.013	199.623	0.8410
Spinner	0.528	28.160	0.1190
Fan blade	0.920	115.134	0.4850
Splitter lip #1	0.070	0.433	0.0018
IGV #1	0.160	1.679	0.0071
Rotor #1	0	0	0
Splitter lip #2	0	0	0
Inner core	0	0	0

TABLE 6.—E^3 IMPINGEMENT STATISTICS FOR A 20 μm MVD LANGMUIR-D DISTRIBUTION

Element	β_{max}	Impingement rate, g/s	Free stream catch fraction
Free stream capture tube (assuming capture area of 3.26 m^2)	1	237.397	1
Inlet lip	0.659	26.574	0.1119
Inlet capture	1.103	190.289	0.8016
Spinner	0.178	6.270	0.0264
Fan blade	1.943	78.901	0.3324
Splitter lip #1	0.164	0.645	0.0027
IGV #1	0.203	2.081	0.0090
Rotor #1	0.176	1.054	0.0044
Splitter lip #2	0.047	0.318	0.0013
Inner core	0.086	0.432	0.0018

TABLE 7.—E^3 IMPINGEMENT STATISTICS FOR A 92 μm MVD SLD DISTRIBUTION WITHOUT SPLASHING

Element	β_{max}	Impingement rate, g/s	Free stream catch fraction
Free stream capture tube (assuming capture area of 3.26 m^2)	1	237.397	1
Inlet lip	0.890	77.401	0.3260
Inlet capture	1.030	199.847	0.8334
Spinner	0.405	24.243	0.1021
Fan blade	1.140	108.041	0.4451
Splitter lip #1	0.081	0.401	0.0017
IGV #1	0.142	1.860	0.0078
Rotor #1	0.027	0.116	0.0005
Splitter lip #2	0.008	0.056	0.0002
Inner core	0.016	0.061	0.0003

TABLE 8.—E^3 IMPINGEMENT STATISTICS FOR A 92 μm MVD SLD DISTRIBUTION WITH SPLASHING

Element	β_{max}	Impingement rate, g/s	Free stream catch fraction
Free stream capture tube (assuming capture area of 3.26 m^2)	1	237.397	1
Inlet lip	0.886	40.904	0.1723
Inlet capture	1.334	210.935	0.8885
Spinner	1.563	14.662	0.0618
Fan blade	3.057	71.090	0.2995
Splitter lip #1	0.055	0.105	0.0004
IGV #1	1.178	3.828	0.0161
Rotor #1	2.133	1.467	0.0062
Splitter lip #2	0.088	0.304	0.0013
Inner core	1.288	6.946	0.0293

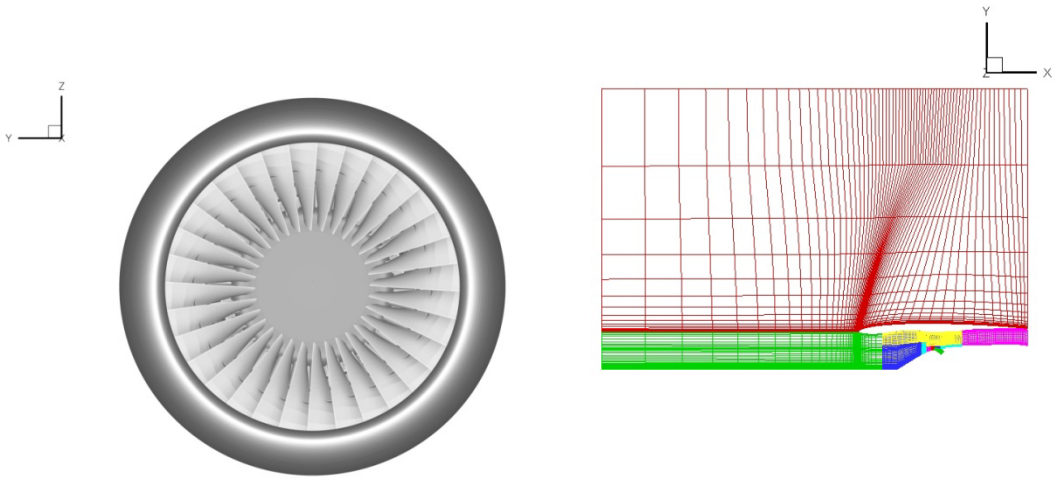

(a) Surface model.

(b) Grid block structure.

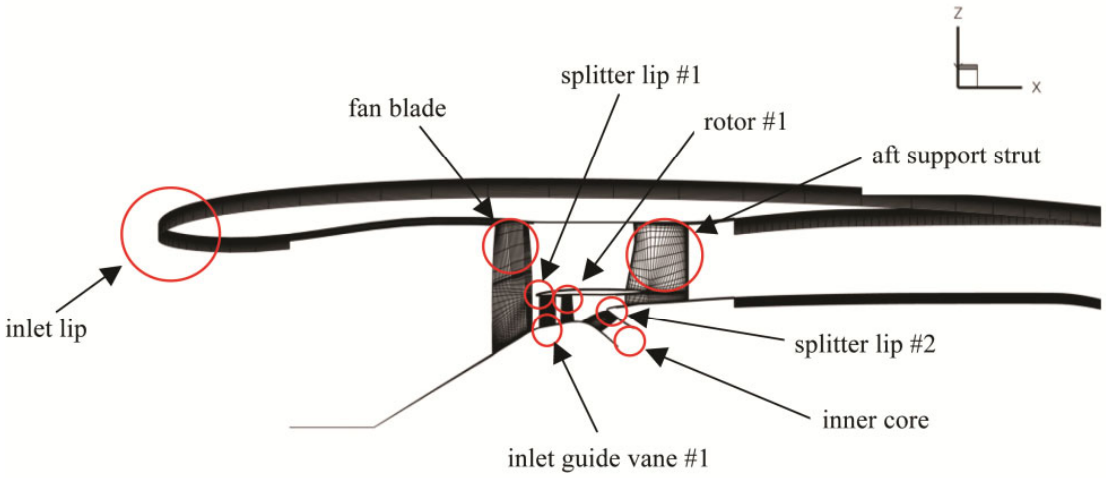

(c) Element designation.

Figure 1.—Surface model and grid structure for E^3 flow model.

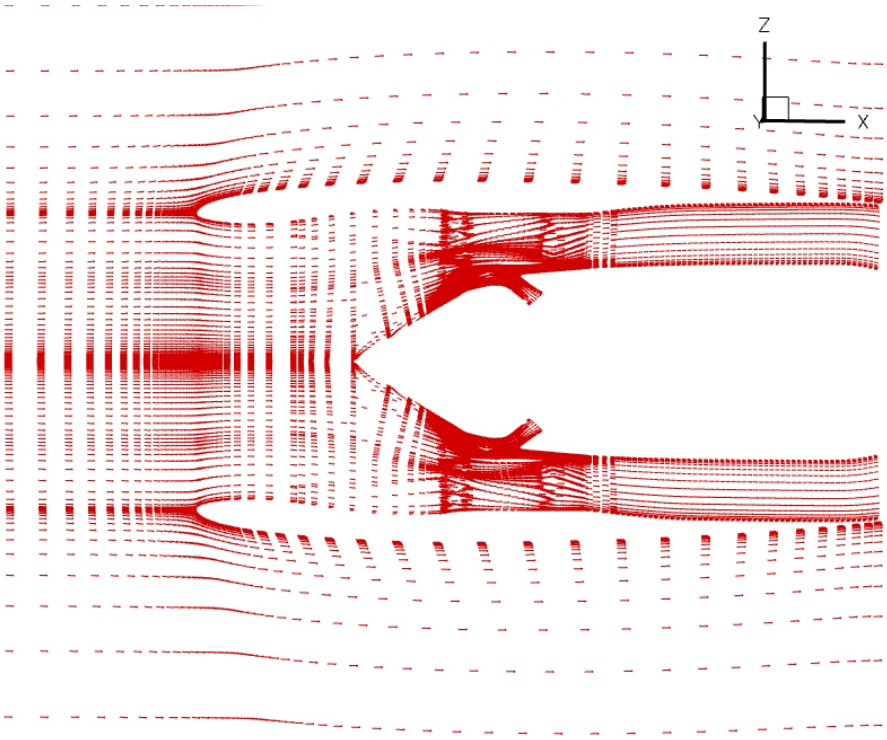

(a) Side view.

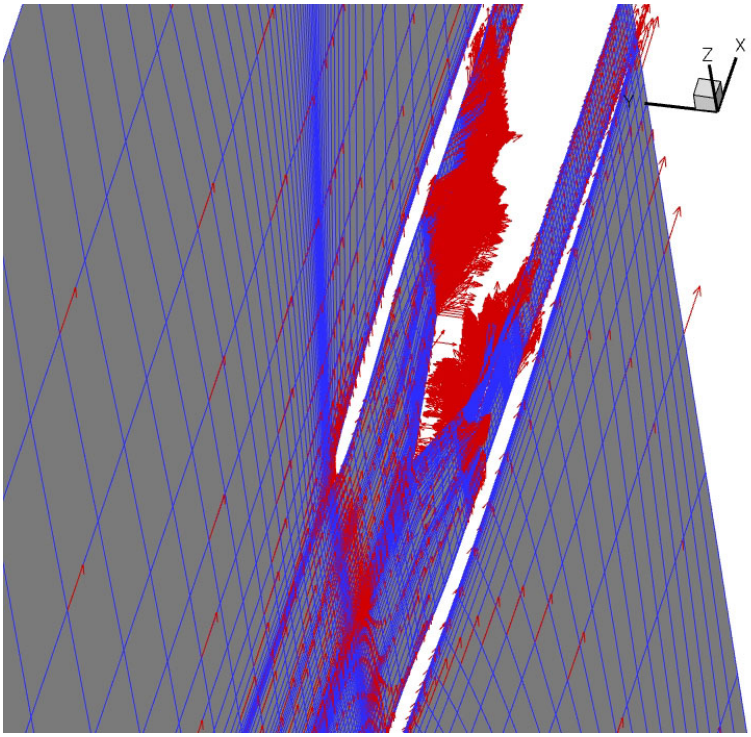

(b) Orthogonal view.

Figure 2.—Centerline velocity vectors for the E^3 low pressure compressor.

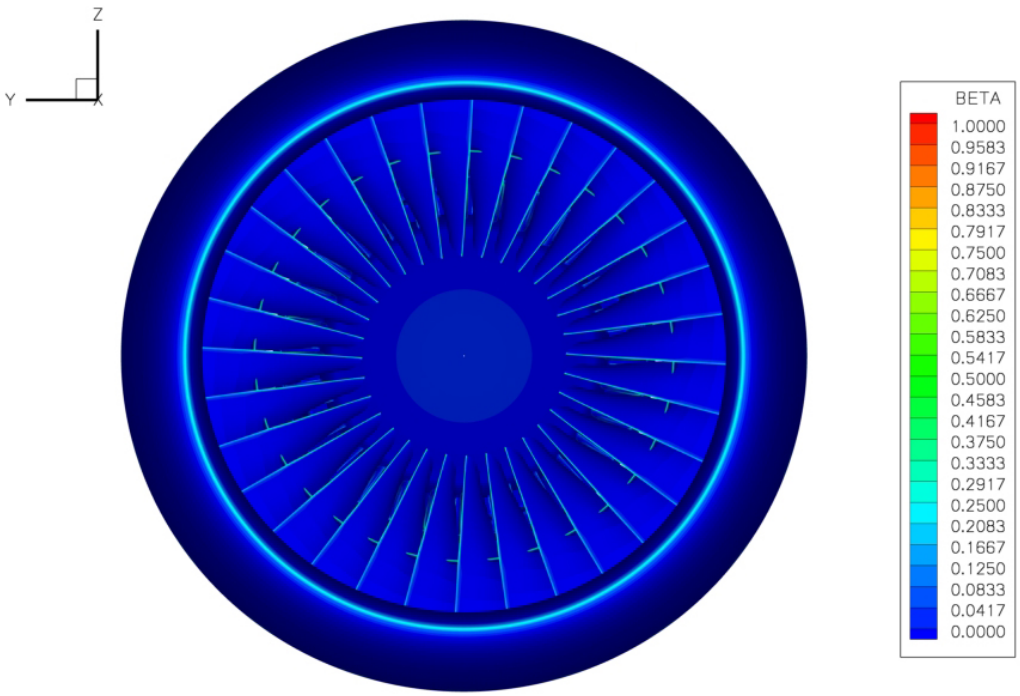

(a) Collection efficiency.

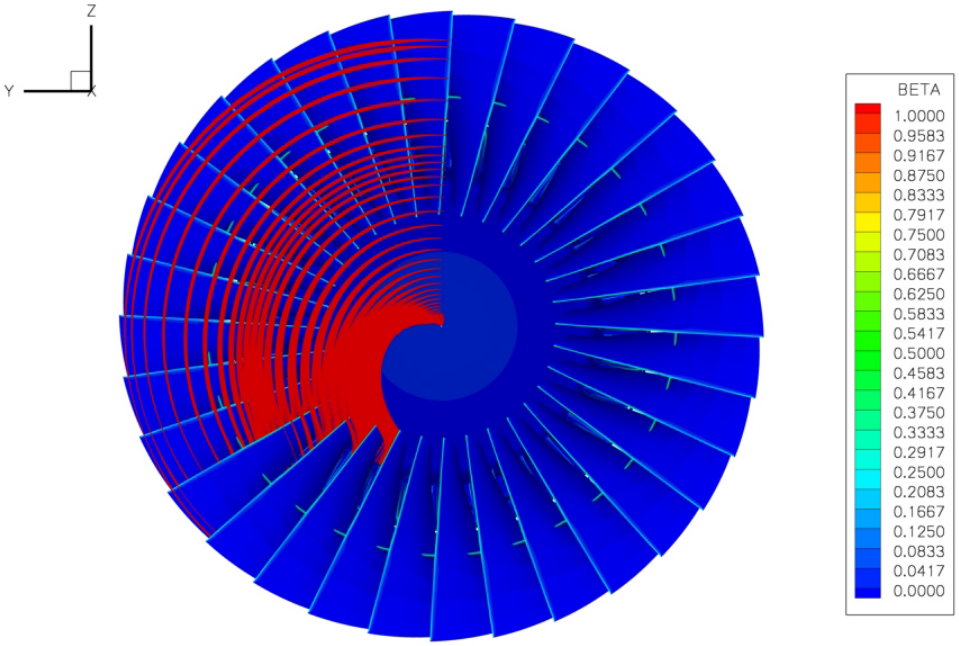

(b) Drop trajectories (front view).

Figure 3.—Drop trajectory and collection efficiency results for the E^3 for 5 μm drop.

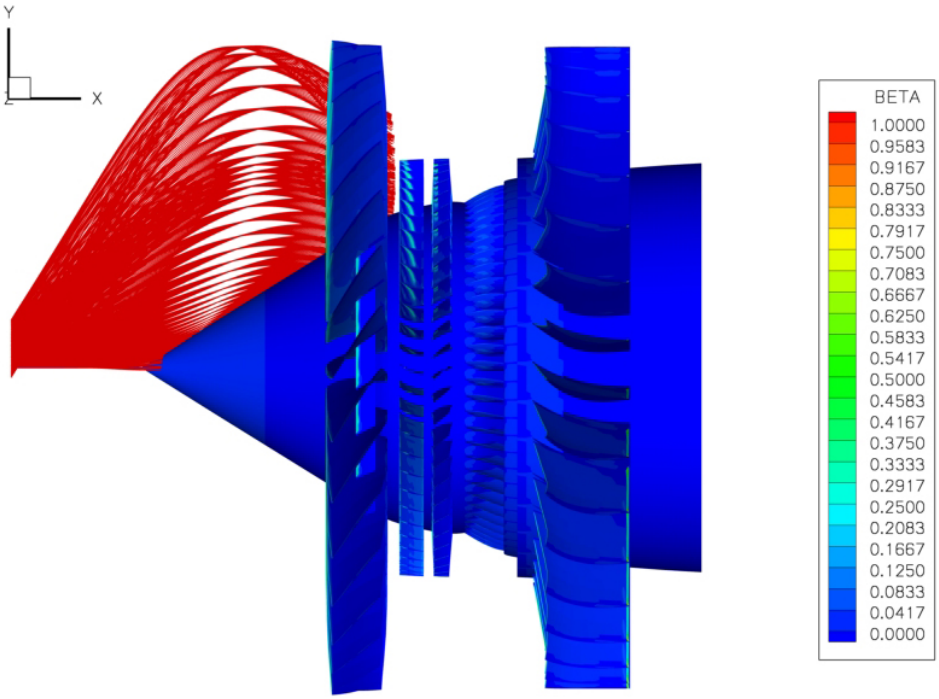

(c) Drop trajectories (axial view).

(d) Drop impact locations (axial view).

Figure 3.—Concluded.

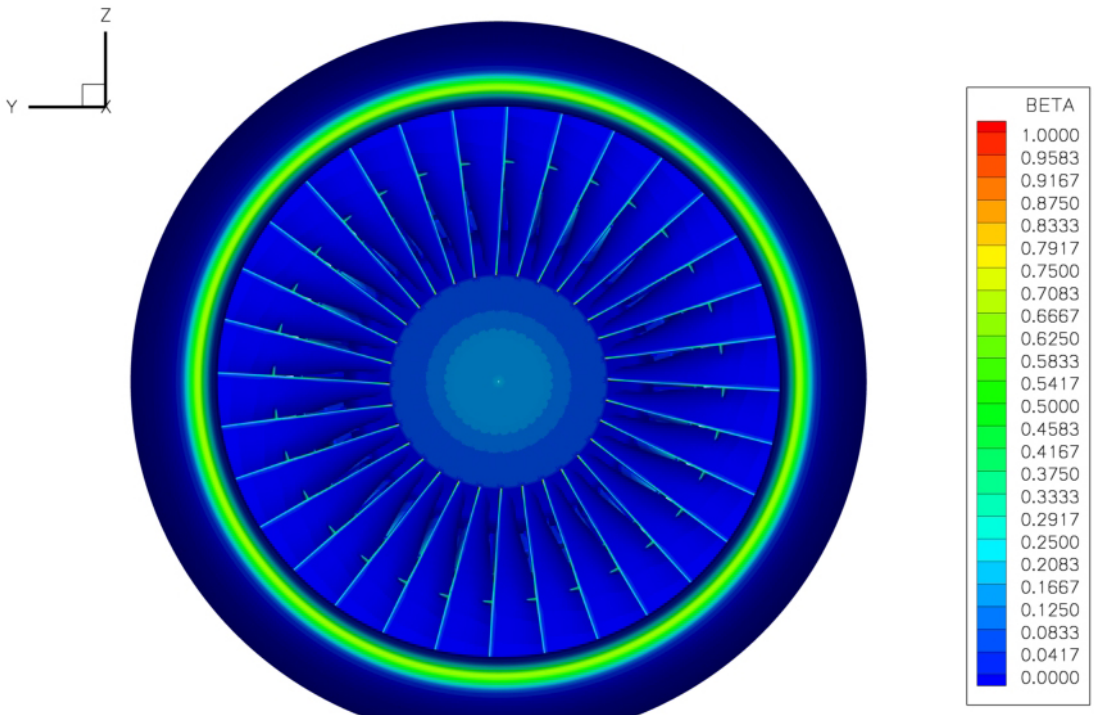

(a) Collection efficiency.

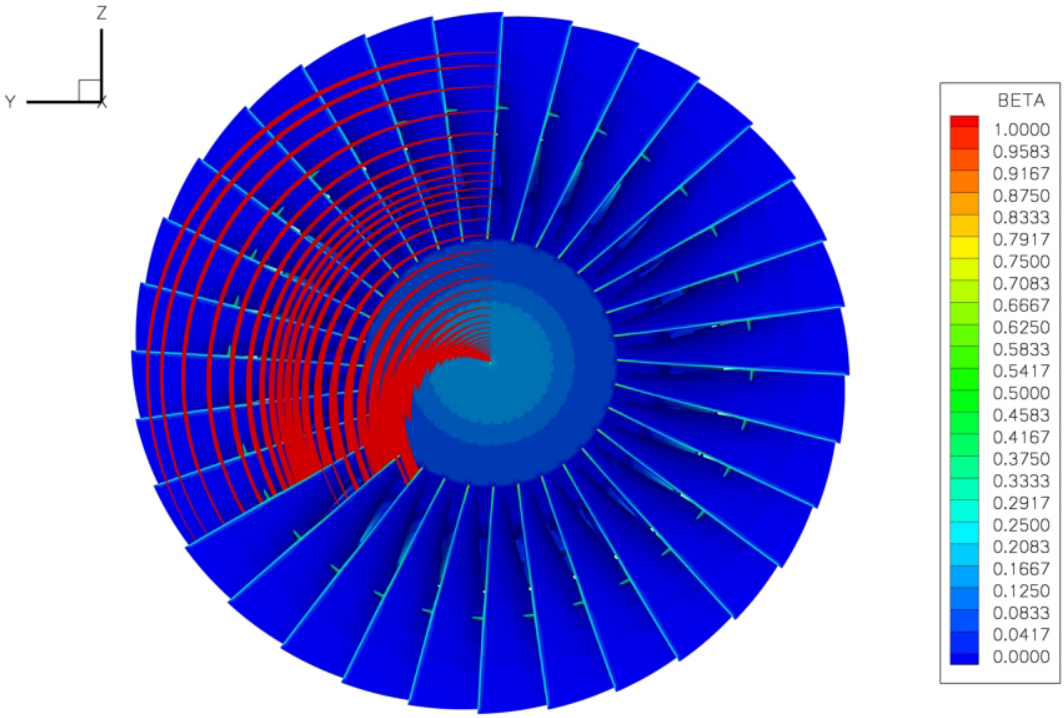

(b) Drop trajectories (front view).

Figure 4.—Drop trajectory and collection efficiency results for the E^3 for 20 μm drop.

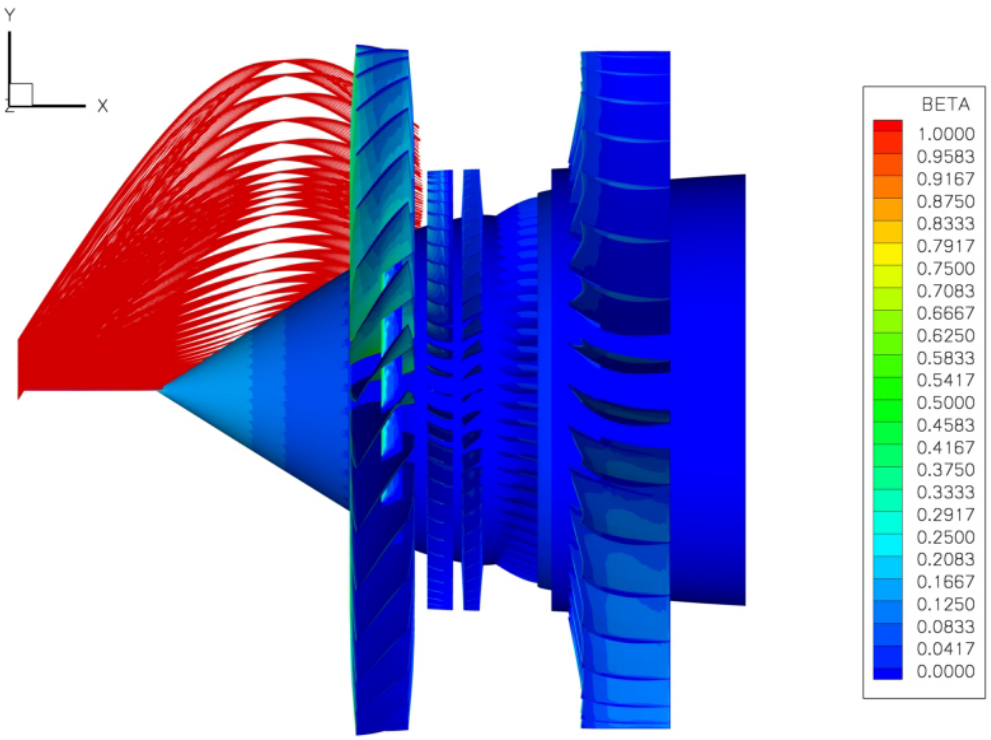

(c) Drop trajectories (axial view).

(d) Drop impact locations (axial view).

Figure 4.—Concluded.

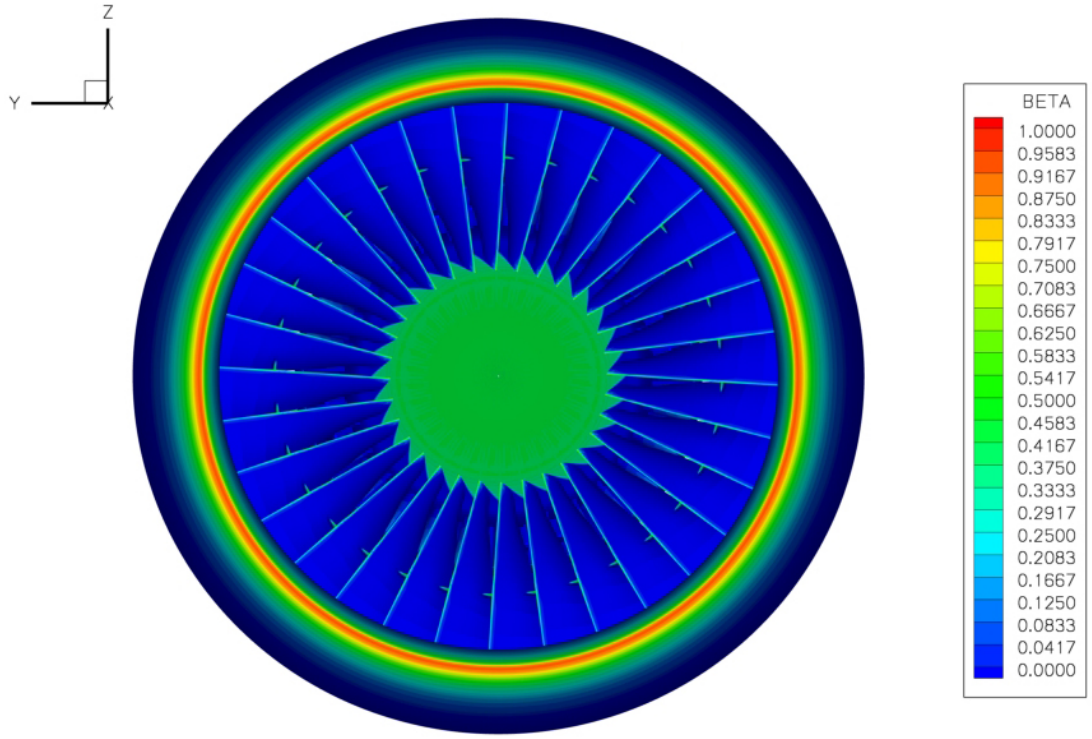

(b) Collection efficiency.

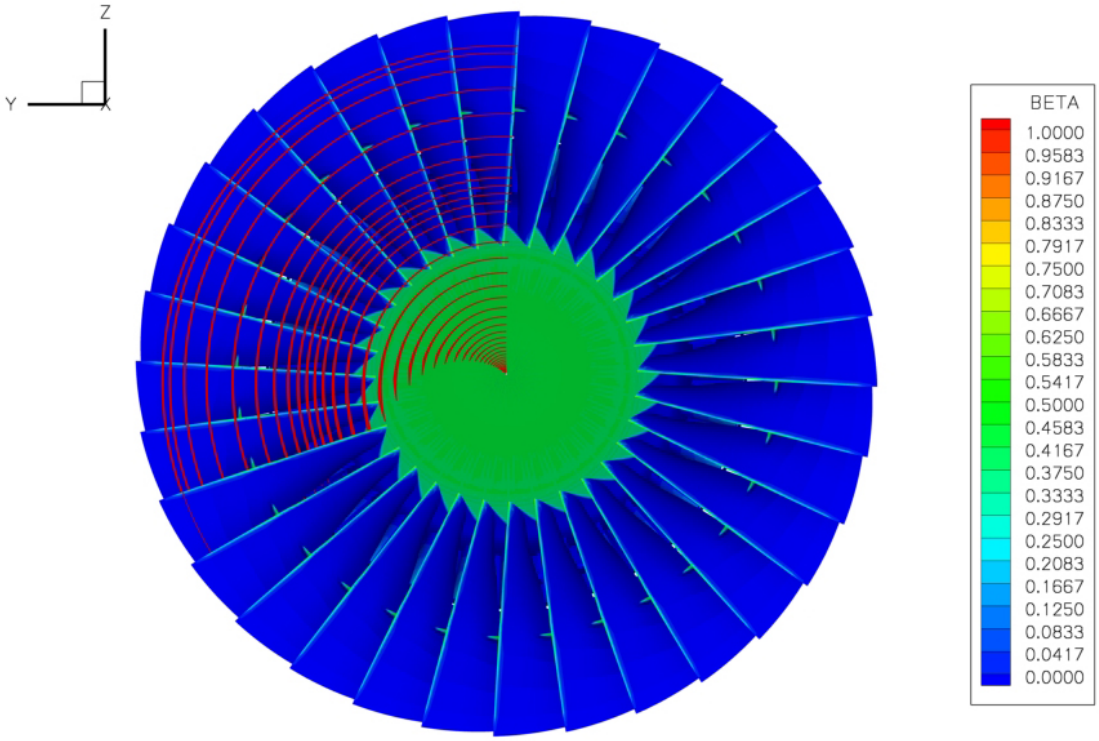

(b) Drop trajectories (front view).

Figure 5.—Drop trajectory and collection efficiency results for the E^3 for 100 μm drop.

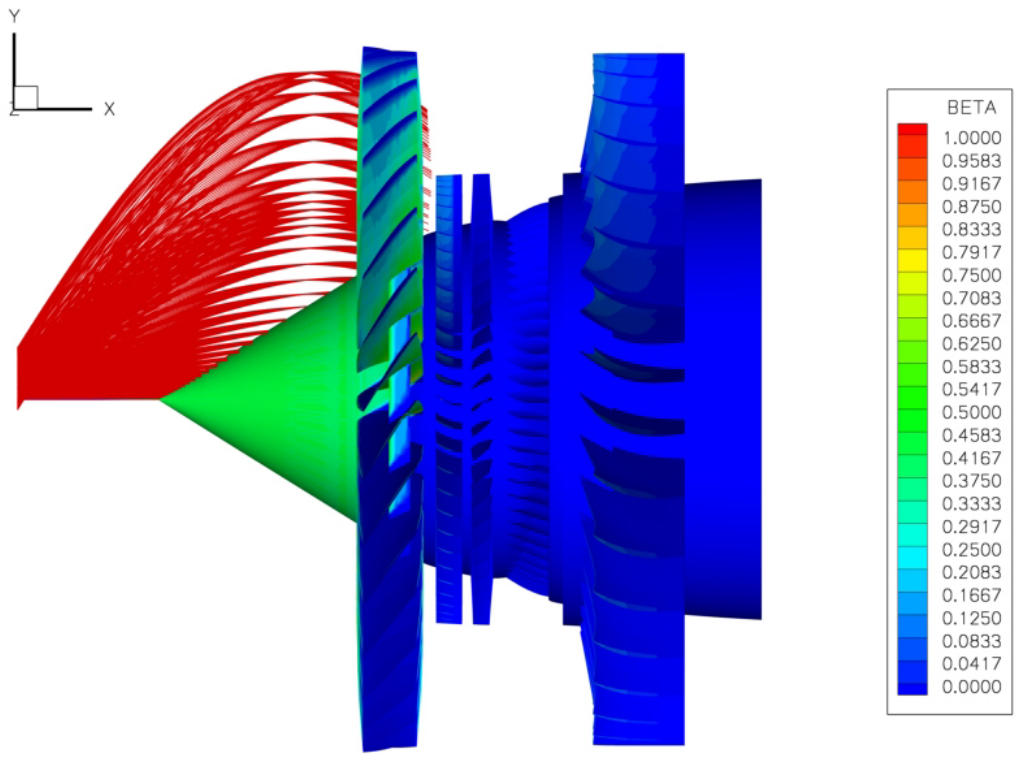

(c) Drop trajectories (axial view).

(d) Drop impact locations (axial view).

Figure 5.—Concluded.

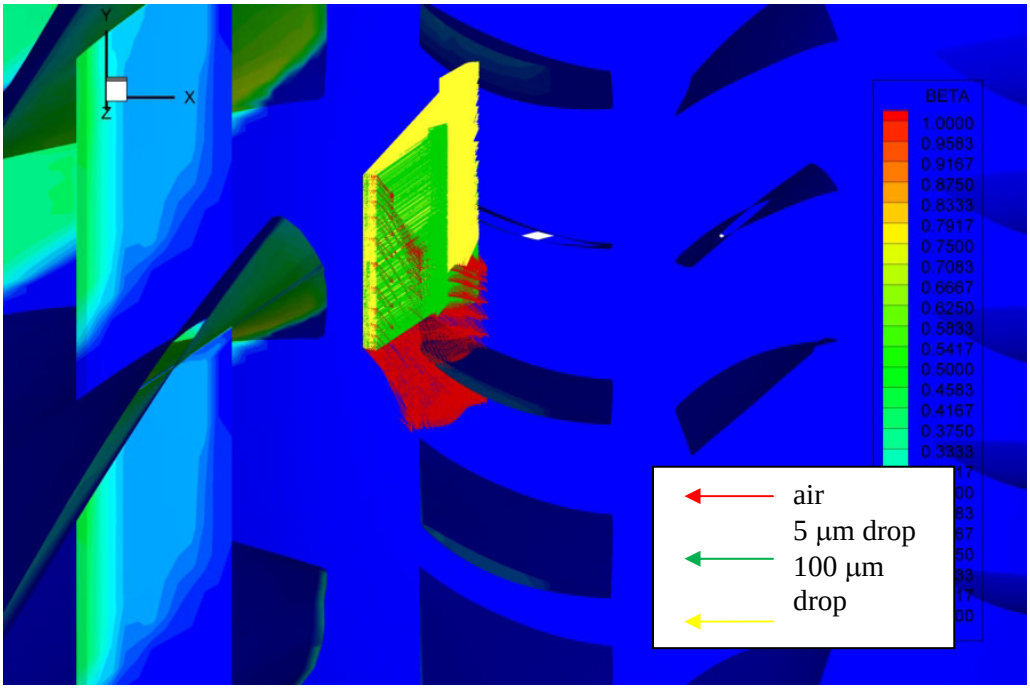

Figure 6.—Velocity vectors and collection efficiency results for the E^3 for 100 μm drop.

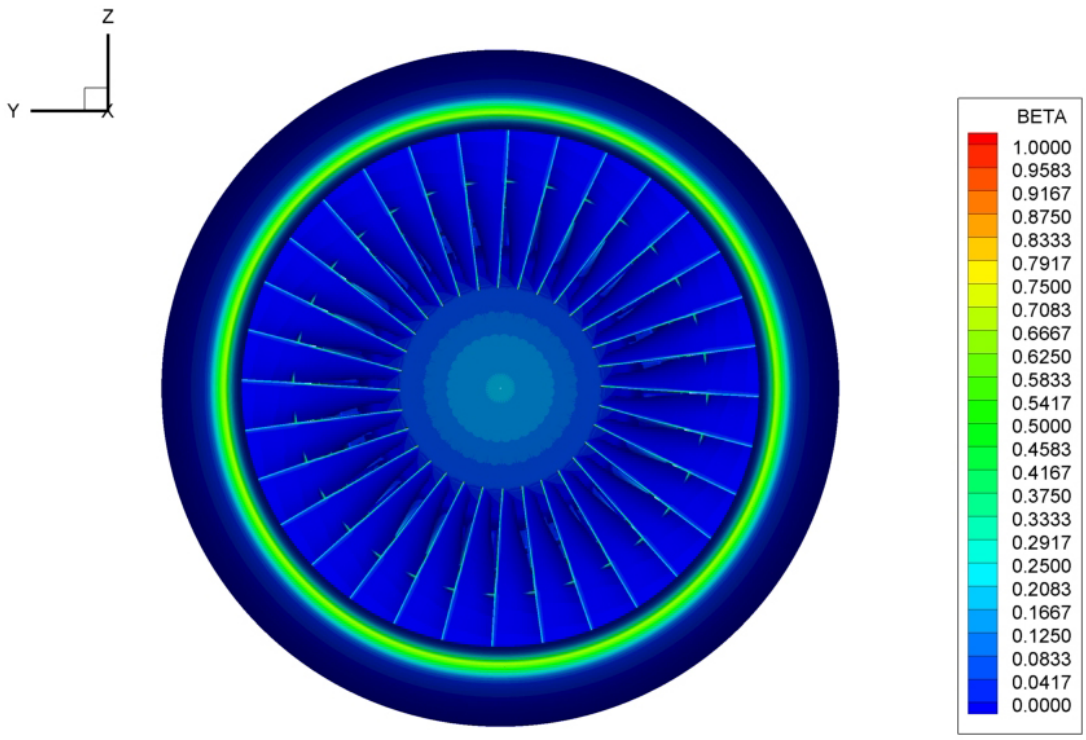

(a) Front view.

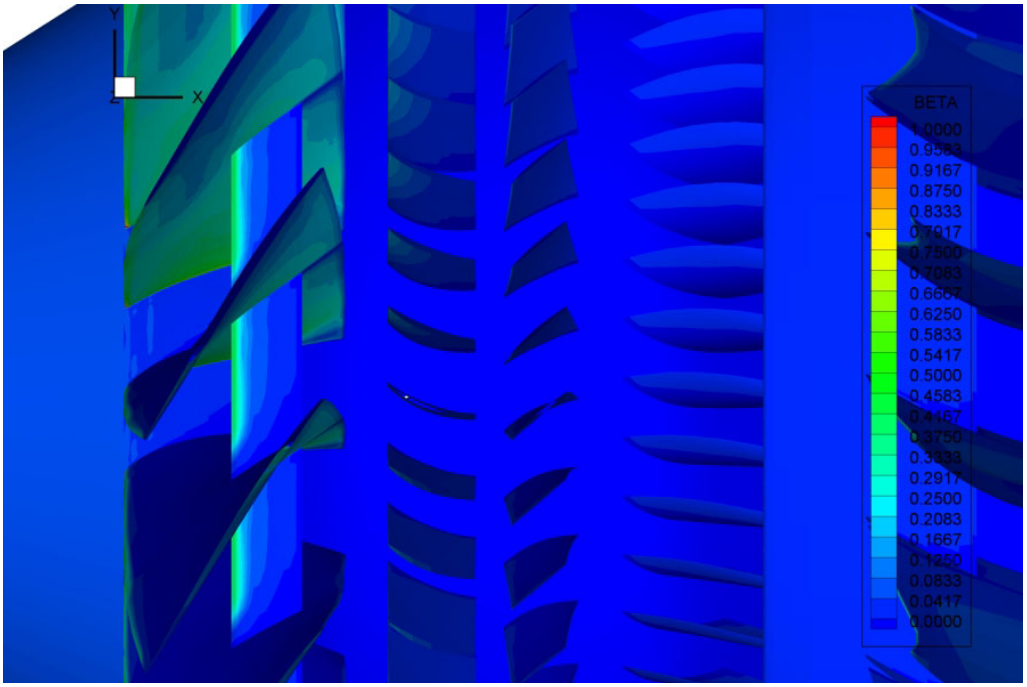

(b) Axial view.

Figure 7.—Collection efficiency results for the E^3 for a 20 μm MVD Langmuir-D distribution.

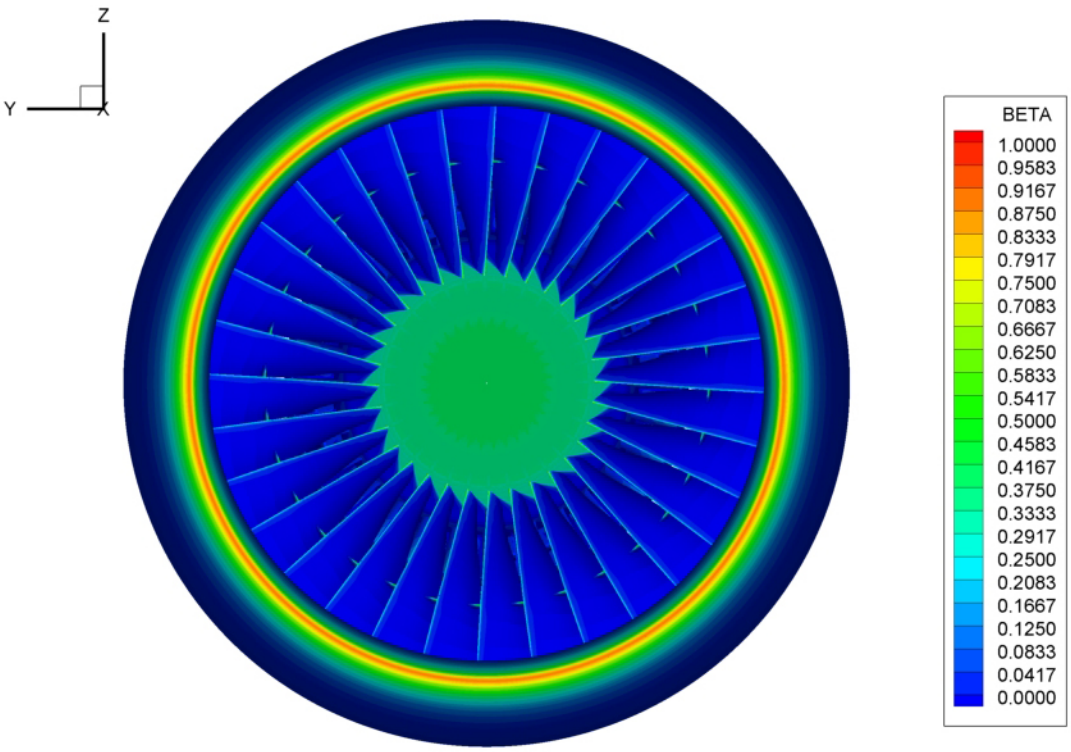

(a) Front view.

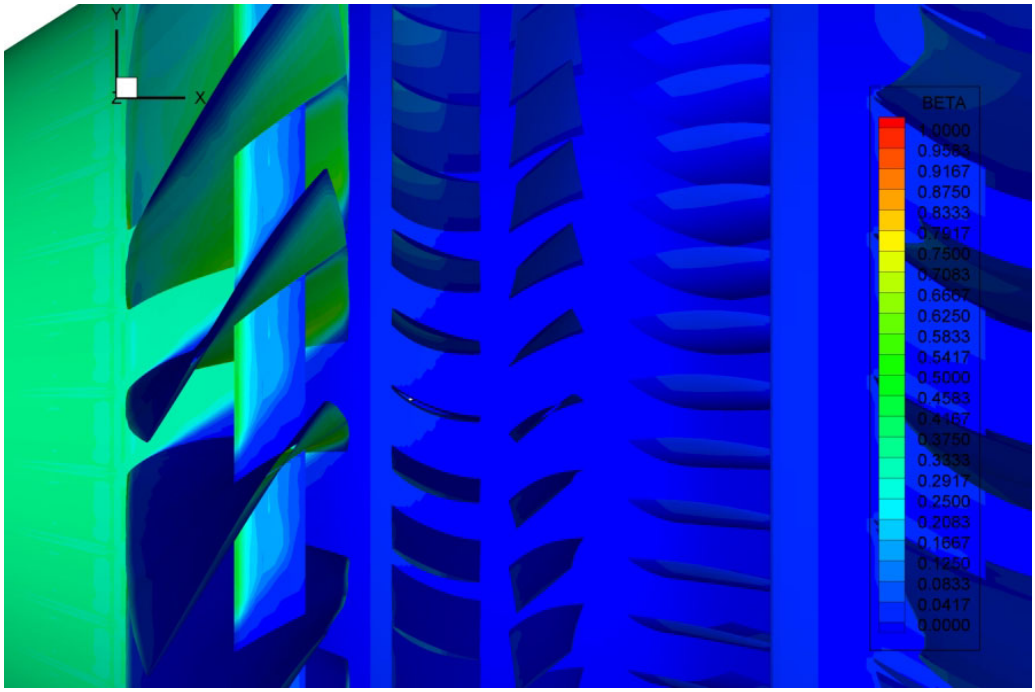

(b) Side view.

Figure 8.—Collection efficiency results for the E^3 for a 92 μm MVD SLD distribution with no splashing.

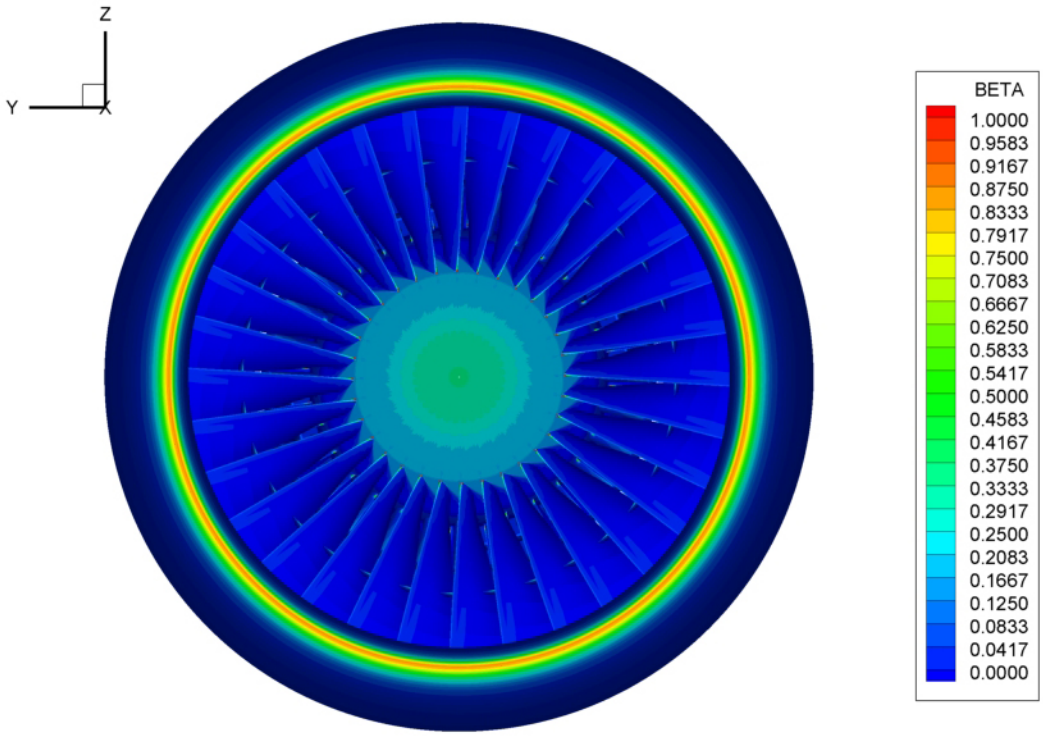

(a) Front view.

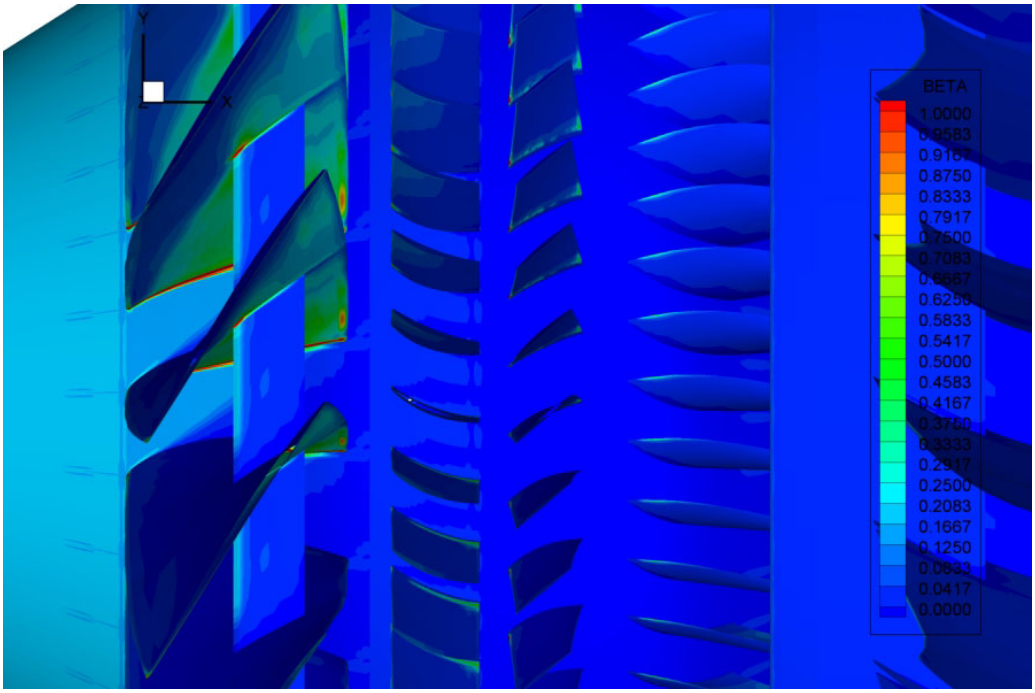

(b) Axial view.

Figure 9.—Collection efficiency results for the E^3 for a 92 μm MVD SLD distribution with splashing.

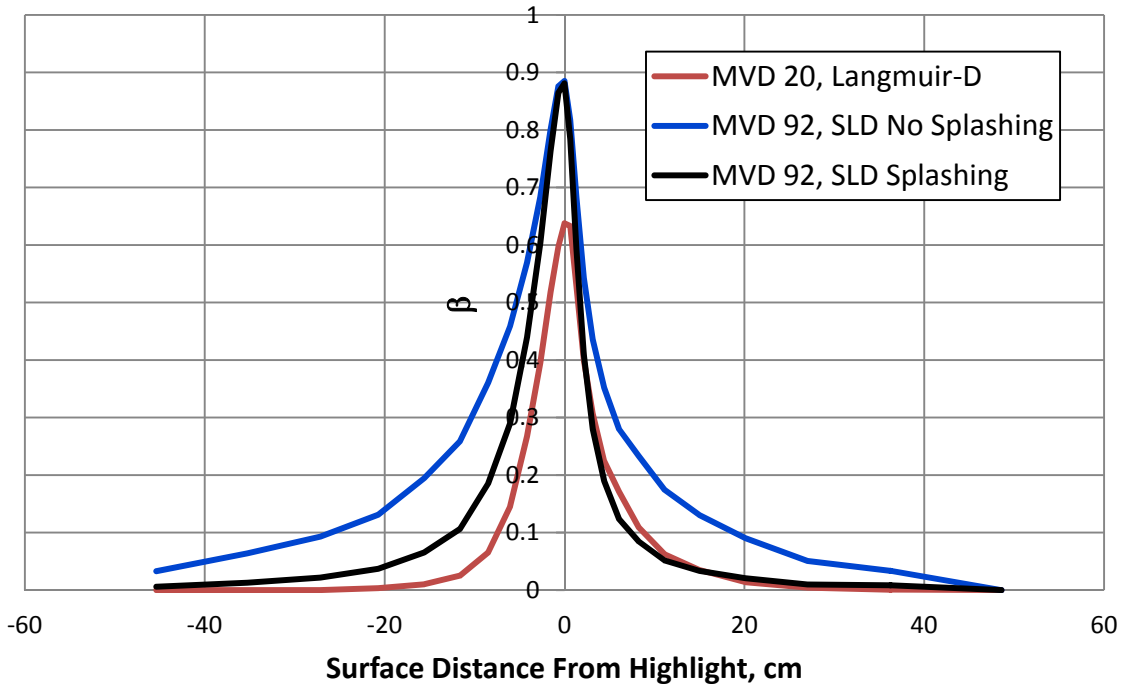

Figure 10.—Collection efficiency distribution for the E^3 inlet lip.

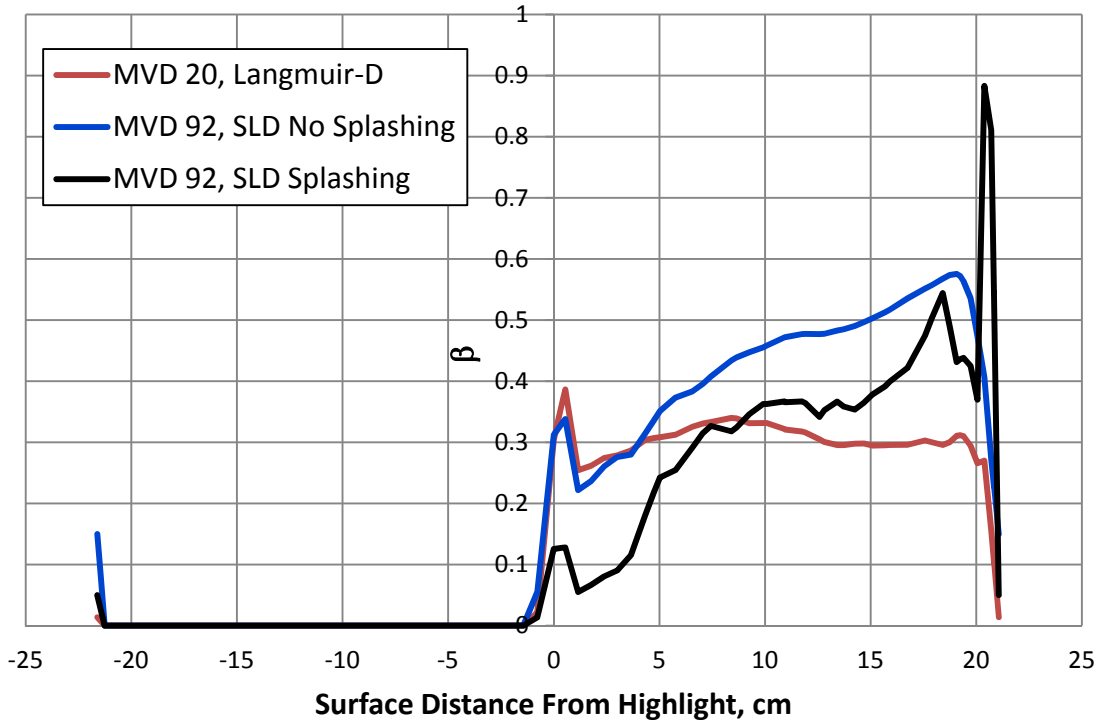

Figure 11.—Collection efficiency distribution for the E^3 fan blade at 25 percent span.

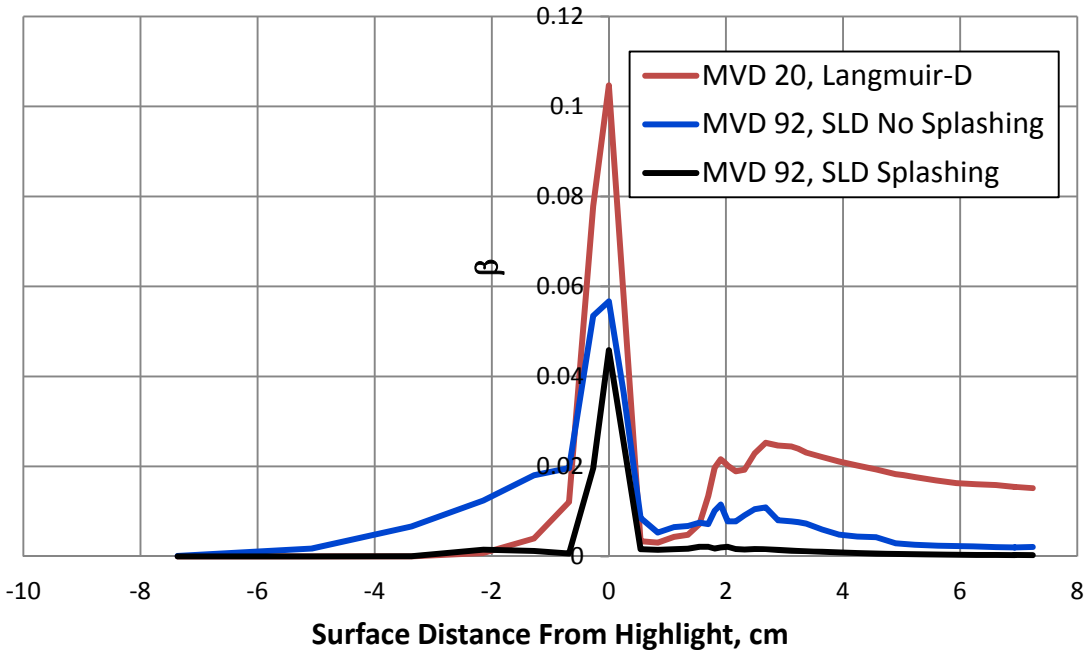

Figure 12.—Collection efficiency distribution for the E^3 splitter lip #1.

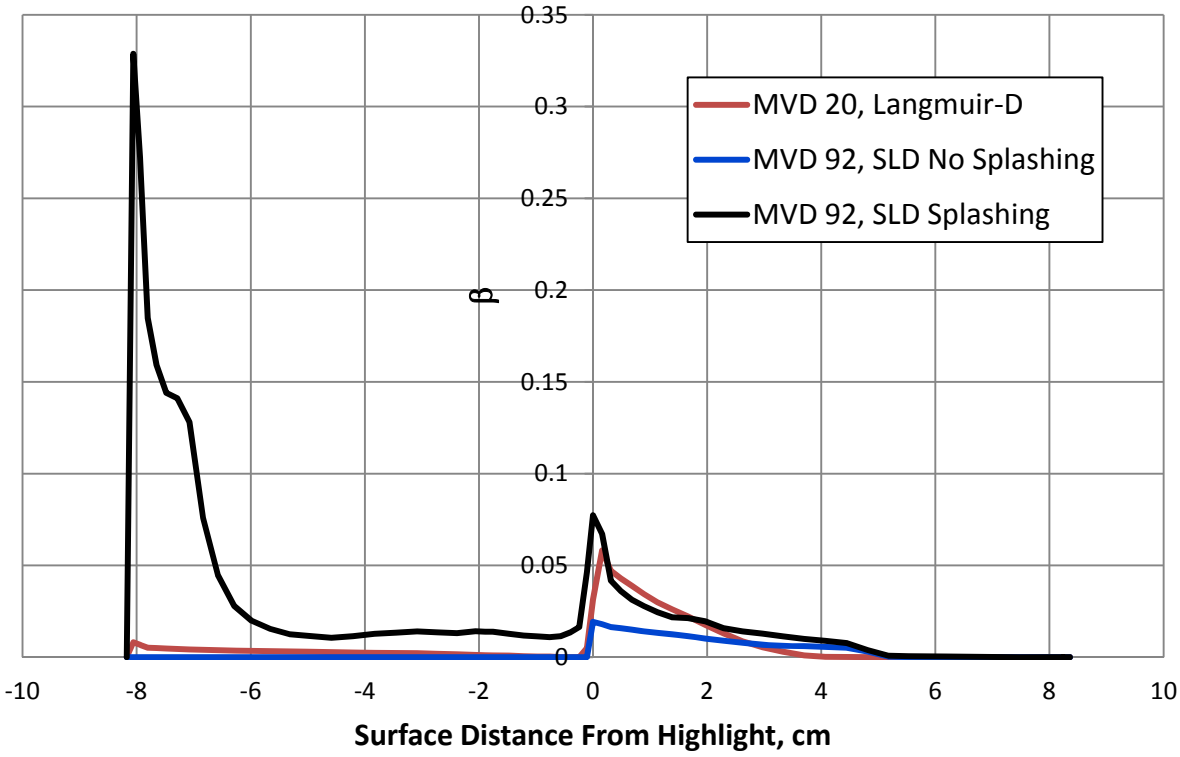

Figure 13.—Collection efficiency distribution for the E^3 IGV #1 at 25 percent span.

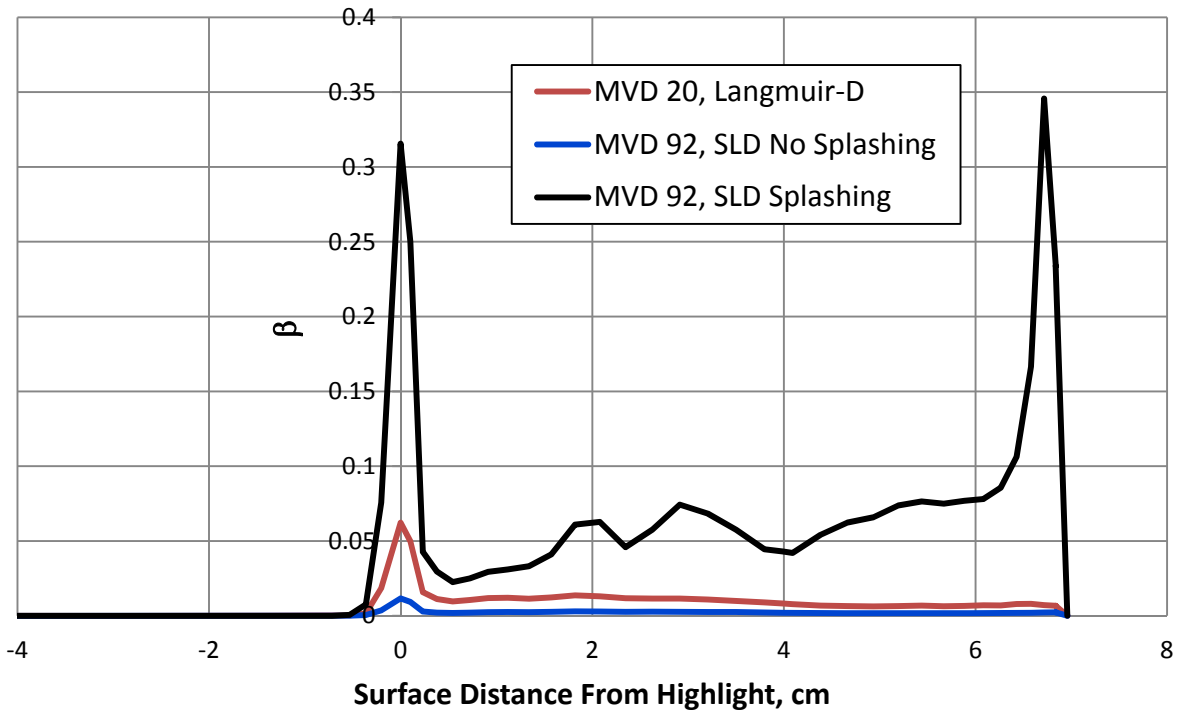

Figure 14.—Collection efficiency distribution for the E^3 rotor #1 at 25 percent span.

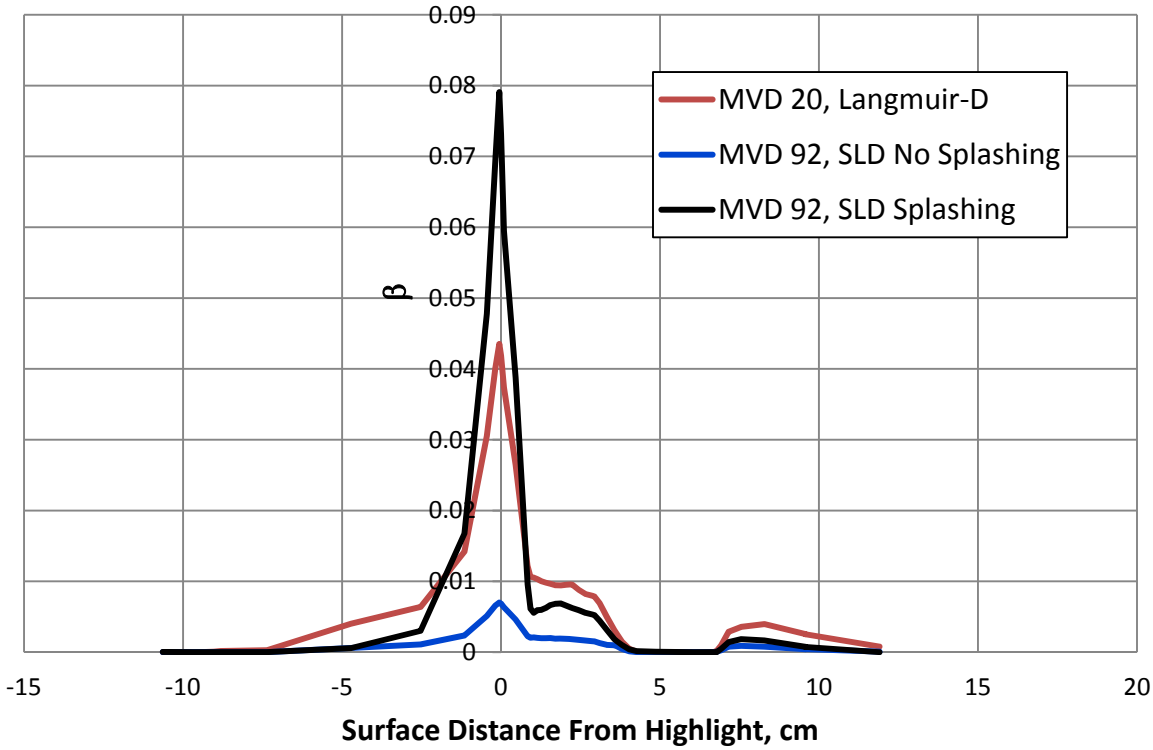

Figure 15.—Collection efficiency distribution for the E^3 splitter lip #2 at 25 percent span.

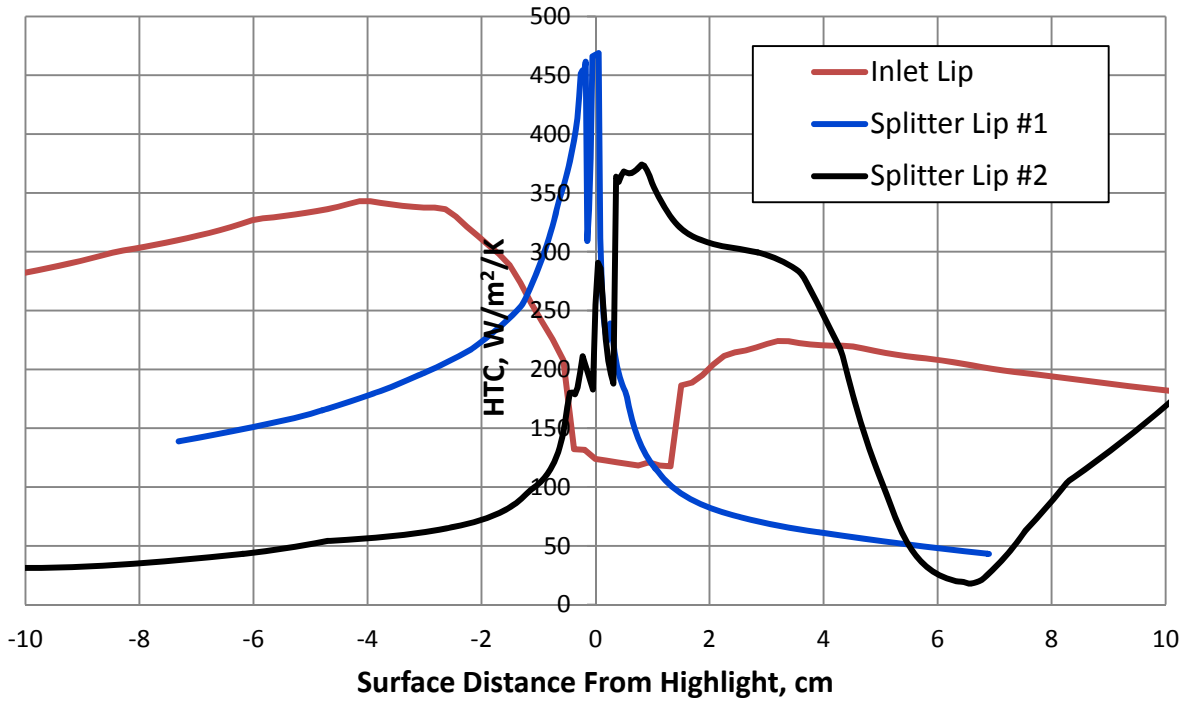

Figure 16.—Heat transfer coefficient distributions for the E^3.

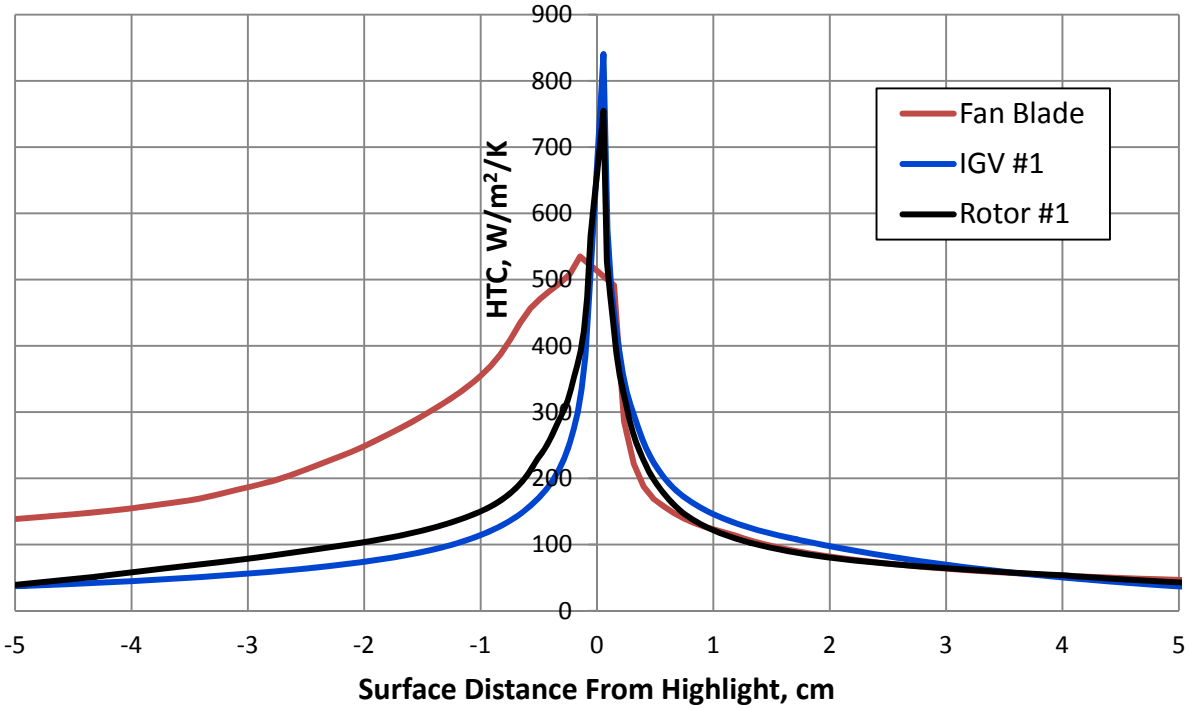

Figure 17.—Heat transfer coefficient distributions for the E^3 blades at 25 percent span.

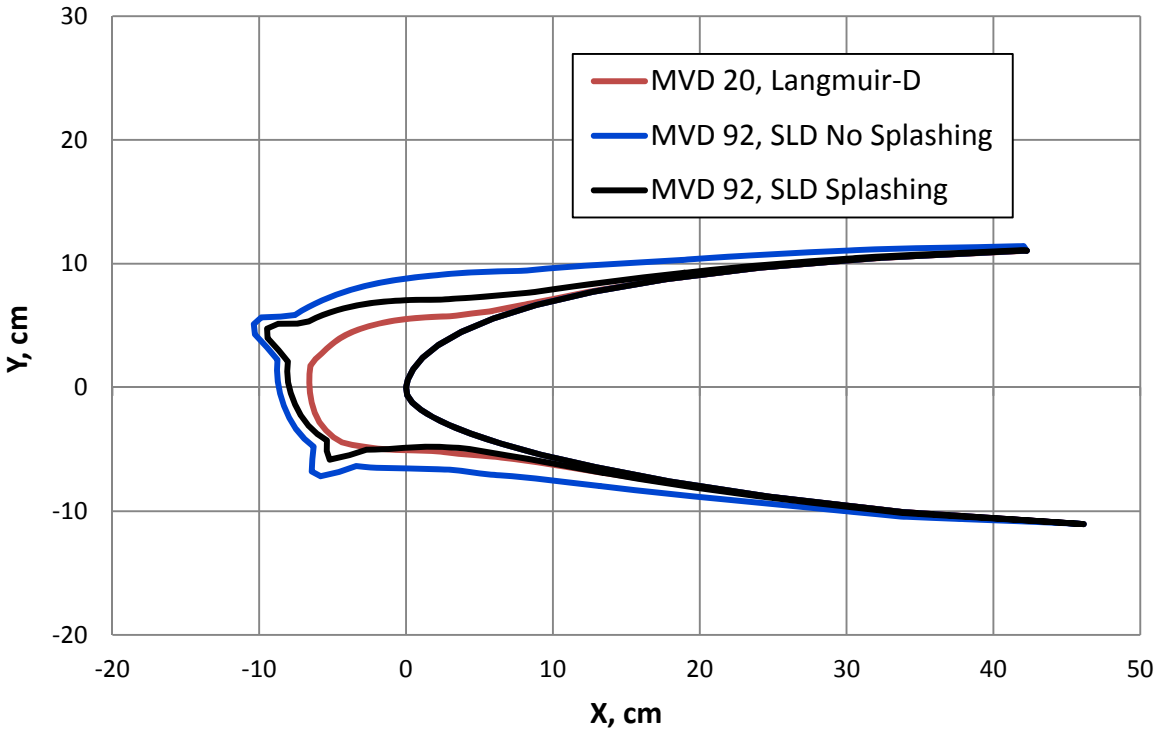

Figure 18.—Ice shapes for the E^3 inlet lip.

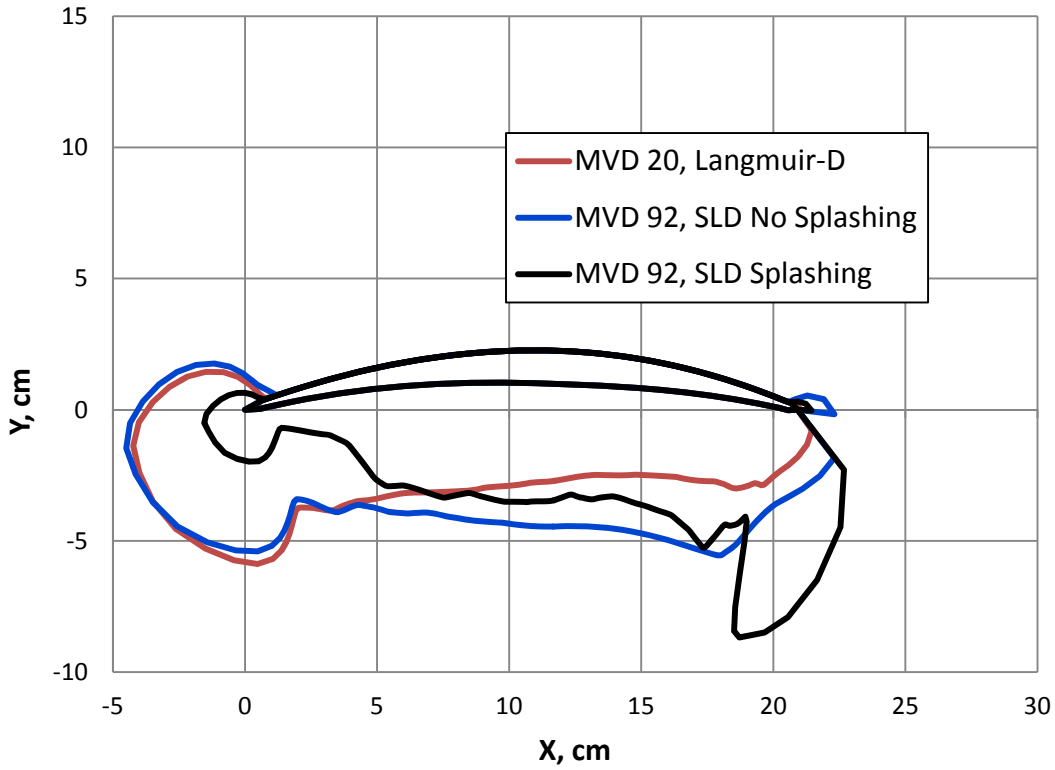

Figure 19.—Ice shapes for the E^3 fan blade.

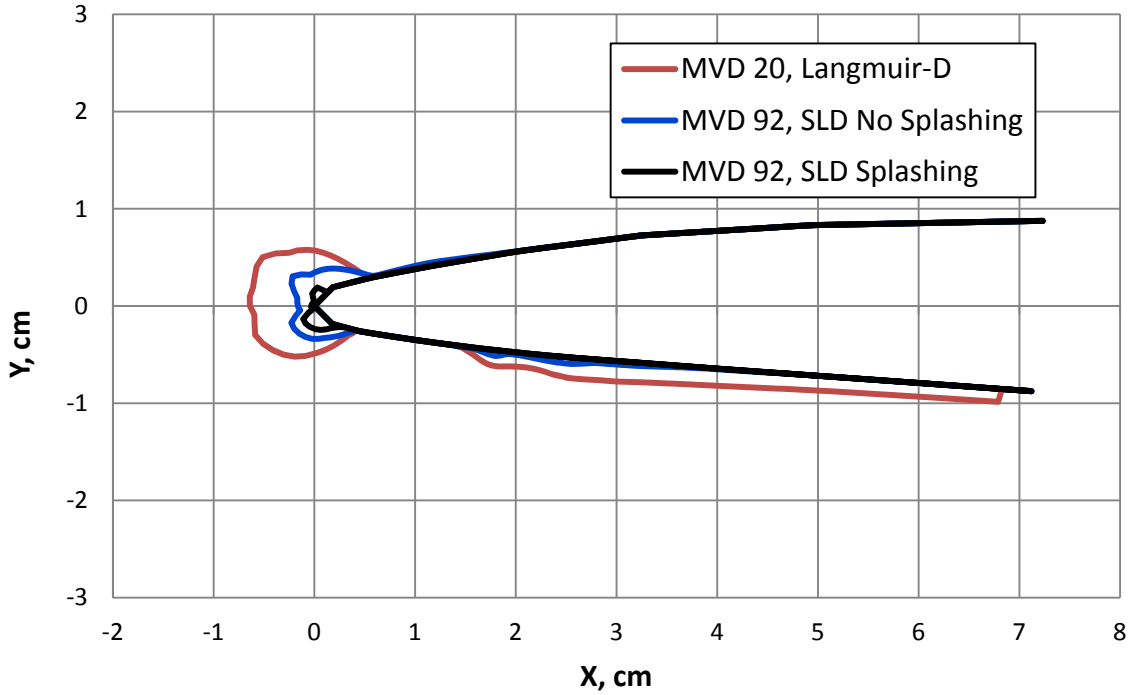

Figure 20.—Ice shapes for the E^3 splitter lip #1.

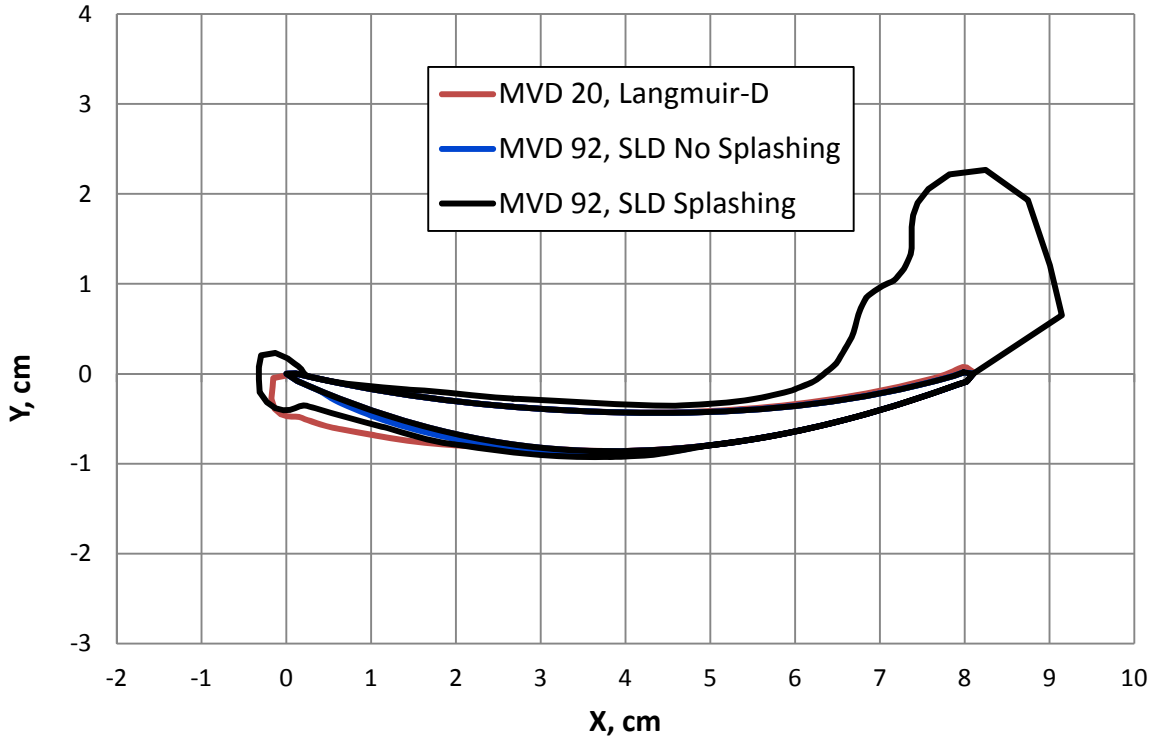

Figure 21.—Ice shapes for the E^3 IGV #1.

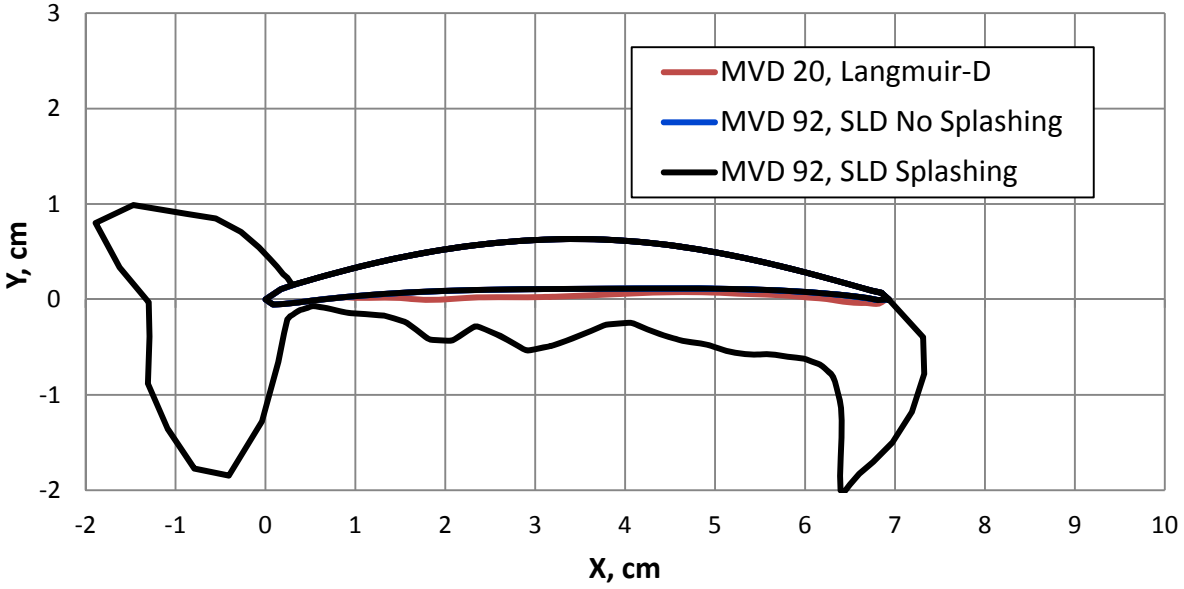

Figure 22.—Ice shapes for the E^3 rotor #1.

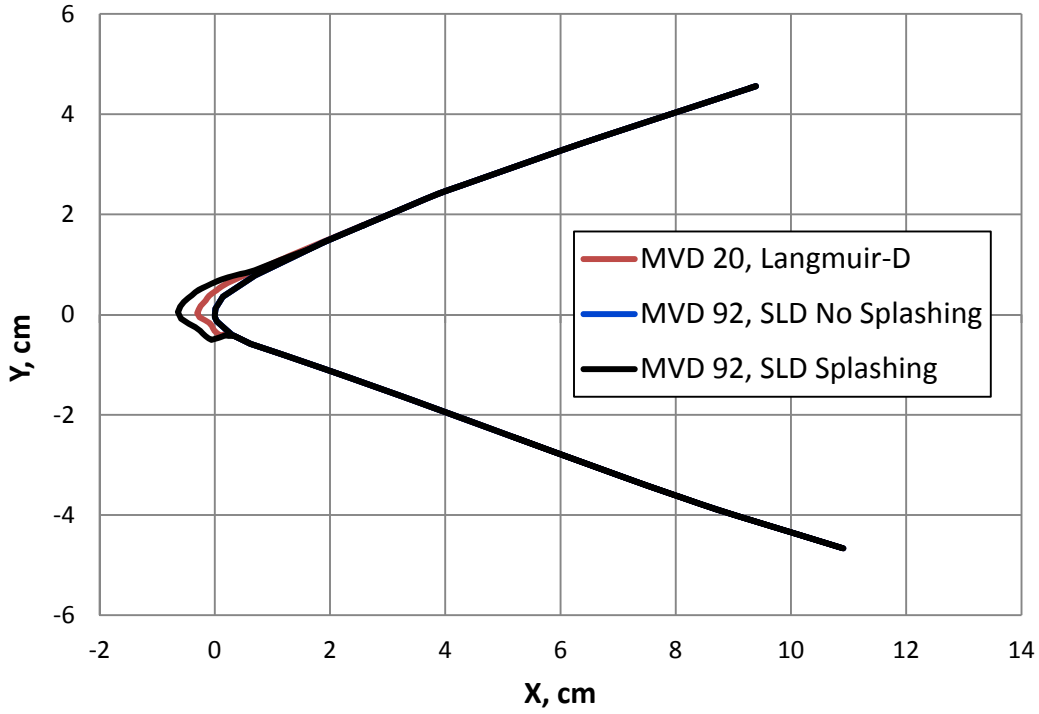

Figure 23.—Ice shapes for the E^3 splitter lip #2.

REPORT DOCUMENTATION PAGE	Form Approved OMB No. 0704-0188

1. REPORT DATE *(DD-MM-YYYY)*	2. REPORT TYPE	3. DATES COVERED *(From - To)*
01-09-2012	Technical Memorandum	

4. TITLE AND SUBTITLE
Particle Trajectory and Icing Analysis of the E^3 Turbofan Engine Using LEWICE3D Version 3

5a. CONTRACT NUMBER

5b. GRANT NUMBER

5c. PROGRAM ELEMENT NUMBER

6. AUTHOR(S)
Bidwell, Colin, S.

5d. PROJECT NUMBER

5e. TASK NUMBER

5f. WORK UNIT NUMBER
WBS 648987.02.03.03.30

7. PERFORMING ORGANIZATION NAME(S) AND ADDRESS(ES)
National Aeronautics and Space Administration
John H. Glenn Research Center at Lewis Field
Cleveland, Ohio 44135-3191

8. PERFORMING ORGANIZATION REPORT NUMBER
E-18383

9. SPONSORING/MONITORING AGENCY NAME(S) AND ADDRESS(ES)
National Aeronautics and Space Administration
Washington, DC 20546-0001

10. SPONSORING/MONITOR'S ACRONYM(S)
NASA

11. SPONSORING/MONITORING REPORT NUMBER
NASA/TM-2012-217696

12. DISTRIBUTION/AVAILABILITY STATEMENT
Unclassified-Unlimited
Subject Category: 03
Available electronically at http://www.sti.nasa.gov
This publication is available from the NASA Center for AeroSpace Information, 443-757-5802

13. SUPPLEMENTARY NOTES

14. ABSTRACT
Particle trajectory and ice shape calculations were made for the Energy Efficient Engine (E^3) using the LEWICE3D Version 3 software. The particle trajectory and icing computations were performed using the new "block-to-block" collection efficiency method which has been incorporated into the LEWICE3D Version 3 software. The E^3 was developed by NASA and GE in the early 1980's as a technology demonstrator and is representative of a modern high bypass turbofan engine. The E^3 flow field was calculated using the NASA Glenn ADPAC turbomachinery flow solver. Computations were performed for the low pressure compressor of the E^3 for a Mach 0.8 cruise condition at 11,887 m assuming a standard warm day for three drop sizes and two drop distributions typically used in aircraft design and certification. Particle trajectory computations were made for water drop sizes of 5, 20, and 100 μm. Particle trajectory and ice shape predictions were made for a 20 μm Langmuir-D distribution and for a 92 mm Super-cooled Large Droplet (SLD) distribution with and without splashing effects for a Liquid Water Content (LWC) of 0.3 g/m^3 and an icing time of 30 min. The E3 fan and spinner combination proved to be an effective ice removal mechanism as they removed greater than 36 percent of the mass entering the inlet for the icing cases. The maximum free stream catch fraction for the fan and spinner combination was 0.60 while that on the elements downstream of the fan was 0.03. The non-splashing trajectory and collection efficiency results showed that as drop size increased impingement rates increased on the spinner and fan leaving less mass to impinge on downstream components. The SLD splashing case yielded more mass downstream of the fan than the SLD non-splashing case due to mass being splashed from the upstream inlet lip, spinner and fan components. The ice shapes generated downstream of the fan were either small or nonexistent due to the small available mass and evaporation except for the 92 μm SLD splashing case. Relatively large ice shapes were predicted for internal guide vane #1 and rotor #1 for the 92 μm SLD splashing case due to re-impingement of splashed mass.

15. SUBJECT TERMS
Icing; CFD; Particle trajectory; Engine icing; LEWICE3D

16. SECURITY CLASSIFICATION OF:			17. LIMITATION OF ABSTRACT	18. NUMBER OF PAGES	19a. NAME OF RESPONSIBLE PERSON
a. REPORT	b. ABSTRACT	c. THIS PAGE			STI Help Desk (email:help@sti.nasa.gov)
U	U	U	UU	38	19b. TELEPHONE NUMBER *(include area code)* 443-757-5802